PHOTODISSOCIATION AND QUANTUM YIELD DETERMINATION OF PEROXYACETYL NITRATE

By

Mark Ernest Angerhofer

RECOMMENDED:

Thomas Clausen

Catherine J. Cahill

Advisory Committee Chair

Thomas Clausen

Department Head

APPROVED:

D Woodall

Dean, College of Science, Engineering and Mathematics

Dean of the Graduate School

6-24-03

Date

PHOTODISSOCIATION AND QUANTUM YIELD DETERMINATION OF PEROXYACETYL NITRATE

A

THESIS

Presented to the Faculty

of the University of Alaska Fairbanks

in Partial Fulfillment of the Requirements

for the Degree of

MASTER OF SCIENCE

By

Mark Ernest Angerhofer, B.S.

Fairbanks, Alaska

August 2003

Abstract

Peroxyacetyl nitrate (PAN) is an important atmospheric species due to its role in global transport of reactive nitrogen oxides, NO_x (= $\cdot NO_2$ + $\cdot NO$). Peroxyacetyl nitrate is formed by reactions involving hydrocarbons and $\cdot NO_2$ in polluted regions and can be transported into the Arctic. To understand the role of PAN as a transporter of NO_x to the Arctic, we need to quantify its decomposition pathways which include: thermal decomposition, photolysis, and reaction with the hydroxyl radical ($\cdot OH$). In colder regions, such as the Arctic, the most rapid decomposition pathway is photolysis. Several photolytic pathways are possible for PAN. We photolyzed PAN in the laboratory using a frequency-doubled tunable dye laser. A highly sensitive technique called cavity ring-down spectroscopy (CRDS) probed the $\cdot NO_3$ produced in the photolysis reaction and we quantified the quantum yield for production of $\cdot NO_3$. The quantum yield is the fraction of photoexcited molecules that decompose to a certain chemical product. We determined that the quantum yield of $\cdot NO_3$ at 289 nm is 0.30 ± 0.08. These results are discussed in context of previous work on PAN photolysis and in terms of a mechanistic model.

Table of Contents

List of Figures

List of Tables

List of Acronyms

APD	Avalanche photodiode detector
CRDS	Cavity ring-down spectroscopy
EG	Ethylene glycol
FTIR	Fourier transform infrared spectroscopy
FWHM	Full width half maximum Gaussian resolution
HPLC	High-performance liquid chromatography
ID	Inner diameter
IR	Infrared
LIF	Laser-induced fluorescence
MPAN	Peroxymethyacrylyl nitrate
Nd:YAG	Neodynium^{3+} yttrium-aluminum garnet
OD	Outer diameter
PAN	Peroxyacetyl nitrate
ppbv	Parts per billion by volume
pptv	Parts per trillion by volume
PPN	Peroxypropionyl nitrate
PN	Peroxy nitrate
sccm	Standard cubic centimeter per minute
UHP	Ultra-high purity
UV	Ultraviolet

Acknowledgements

The National Science Foundation in the form of a CAREER grant (CHE-00-94038) awarded to Dr. William Simpson has provided funding that has allowed me to perform this exciting research and to gain access to state of the art equipment.

I would also like to thank Kelly Vaughan for making the PAN samples and my colleague Tamoki Nakayama for his help and insights in the lab.

I am also thankful for having the opportunity to work with many smart and talented people in the UAF Chemistry Department including my committee members Dr. Tom Clausen and Dr. Catherine Cahill. I owe a special thanks to Shelia Chapin for her help.

I would also like to thank my adviser Dr. William Simpson for the opportunity to work on this project and for providing his invaluable mentoring and guidance.

Most of all, I would like to thank my family for always providing encouragement and support.

Chapter 1

Atmospheric chemistry of peroxyacetyl nitrate (PAN)

1.1 Introduction

Peroxyacetyl nitrate (PAN) was discovered in the 1950's by Stephens and co-workers while conducting infrared spectroscopy on polluted air [*Stephens*, 1987]. They observed new infrared absorption bands while studying ozone formation. It took several years to determine that these bands corresponded to a family of peroxy nitrate (PN) compounds. Peroxyacetyl nitrate is typically the most atmospherically abundant compound in the family. The chemical formula of PAN is $CH_3C(O)OONO_2$, and its structure is shown in figure 1.1. Other members of the PN family are peroxypropionyl nitrate (PPN, $C_2H_5C(O)OONO_2$), peroxybenzoyl nitrate (PBzN, $C_6H_5C(O)OONO_2$) peroxymethyacrylyl nitrate (MPAN, $CH_2=C(CH_3)C(O)OONO_2$) and peroxy(hydroxyl)acetyl nitrate (HPAN, $HOCH_2C(O)OONO_2$). All of these compounds fit the general formula $R\text{-}C(O)OONO_2$ where R is an organic group. The second most abundant peroxy nitrate compound is PPN, which is present in the atmosphere at concentration levels typically 5-10% of that of PAN [*Singh*, 1987]. Other members in the PN family, MPAN and HPAN, can be formed by the oxidation of isoprene (a volatile plant hormone). This thesis focuses on PAN because it is typically the most abundant and important species within the PN family.

Peroxyacetyl nitrate is an important atmospheric species due to its role in the transport and global distribution of nitrogen oxides, NO_x ($= \cdot NO_2 + \cdot NO$). Peroxyacetyl nitrate is produced in pollution plumes. It then may transport and decompose, releasing NO_x far from its original source. Therefore, PAN acts as a storage reservoir for NO_x. The chemistry of NO_x affects most chemical processes in the atmosphere, thus PAN affects the global atmosphere [*Moxim et al.*, 1996].

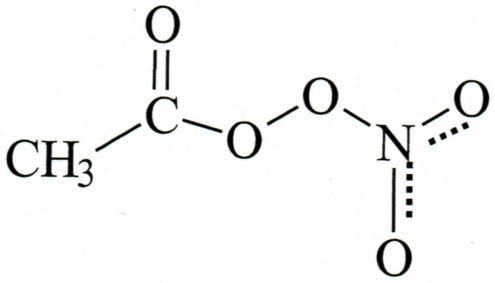

Figure 1.1 The chemical structure of peroxyacetyl nitrate (PAN).

A critical parameter for understanding PAN's role as a transporter of NO_x is its lifetime. The lifetime is the amount of time PAN remains in the environment and is controlled by a combination of PAN's sink processes: thermal decomposition, reaction with the hydroxyl radical (·OH), and photolysis. A better understanding of these PAN sinks helps to understand its distribution and fate in the atmosphere. Thermal decomposition and reaction with ·OH have been studied while photolysis has received little attention. Photolysis is a particularly important process in cold regions (*i.e.* the Arctic) because thermal processes are slow in these environments. Thus, it is important to understand the photolysis of PAN which is the goal of this research. This chapter discusses the formation, transport, and sinks of PAN.

1.2 Formation

Peroxyacetyl nitrate has no known direct emission sources. It forms by chemical reactions in the atmosphere involving oxidation of hydrocarbon precursors, sunlight and $\cdot NO_2$. The hydrocarbons and $\cdot NO_2$ that form PAN come primarily from anthropogenic sources such as fossil fuel combustion and biomass burning [*Singh*, 1987]. An example of PAN formation from an aldehyde precursor (a common product of hydrocarbon oxidation) follows the reaction sequence

$$CH_3C(O)H + h\nu \rightarrow CH_3C(O)\cdot + H\cdot \qquad (1.1)$$

$$CH_3C(O)\cdot + M + O_2 \rightarrow CH_3C(O)OO\cdot + M^* \qquad (1.2)$$

$$CH_3C(O)OO\cdot + M + \cdot NO_2 \rightleftharpoons CH_3C(O)OONO_2 + M^* . \qquad (1.3)$$

In reaction 1.1, $h\nu$ represents an absorption of a photon. In reactions 1.2 and 1.3, M represents a molecule that acts as a collisional quencher to stabilize the combination products shown. Following the reaction, the collisional quencher, M, carries off energy and is shown as an energized form, M^*. *DeMore et al.* [1997] report for reaction 1.3 a high pressure limit rate constant, $k_{\infty(1.3)}$, of 9.3×10^{-12} cm^3 molecule^{-1} s^{-1} at 300 K and an

associated low pressure limit rate constant, $k_{0(1.3)}$, of 9.7 x 10^{-29} cm^6 $molecule^{-2}$ s^{-1} at 300 K. At high pressures (> 100 Torr) a collision with M always occurs during the lifetime of the addition complex. Therefore, the reaction appears to be second order overall with a rate coefficient, k_∞. At low pressures, the collisional quenching step becomes rate limiting and the overall rate appears as third order with a rate coefficient, k_0. The formation of PAN (reaction 1.3) is reversible and PAN can dissociate to $\cdot NO_2$ and the peroxyacetyl radical ($CH_3C(O)OO\cdot$). The reverse of reaction 1.3 depends strongly on temperature and the Arrhenius rate expression in the high pressure limit, $k_{\infty(1.3rev)}$, is 5.4 x 10^{16} s^{-1} exp (-13830 K /*T*) where *T* is temperature [*Finlayson-Pitts and Pitts*, 2000]. The associated low pressure Arrhenius rate expression, $k_{0(1.3rev)}$, is 4.9 x 10^{-3} s^{-1} cm^3 $molec^{-1}$ exp (-12100 K /*T*) [*Finlayson-Pitts and Pitts*, 2000]. At 300 K the equilibrium constant for reaction 1.3 in the high pressure limit, $K_{\infty(eq)(1.3)}$, is 1.8 x 10^{-8} cm^3 $molecule^{-1}$. This value of $K_{\infty(eq)(1.3)}$ indicates that for concentrations of $\cdot NO_2$ > 5 x 10^7 molecules cm^{-3} (2 pptv at 1 atm and 298 K), PAN is more thermodynamically stable than $CH_3C(O)OO\cdot$ and $\cdot NO_2$. As temperatures cool, $K_{\infty(eq)(1.3)}$ increases, increasing the stability of PAN.

1.3 Transport

The role of PAN as a carrier for NO_x has led researchers to study its transport around the globe [*Walega et al.*, 1992; *Moxim et al.*, 1996; *Jacob et al.*, 1996]. In polluted air masses such as Los Angeles, mixing ratios of PAN as high as 30 ppbv have been measured [*Holmes*, 1987]. As air from these polluted areas uplifts, it cools, thereby increasing the stability of PAN and allowing it to transport long distances. Upon descent, the air warms, decreasing PAN's stability, and releasing NO_x into otherwise clean environments.

Wintertime wind patterns can transport PAN into the Arctic. In the winter, high-pressure cells form over continental regions while low pressure cells form in the Northern

Pacific (the Aleutian low) and the Northern Atlantic (the Icelandic low). The Icelandic low produces westerly wind patterns over the North Atlantic that can carry PAN and its precursors from eastern North America into the high Arctic. Also, southerly winds over the Norwegian Sea can pump polluted urban air masses from cities in Europe into the Arctic. The Aleutian low over the Northern Pacific can steer air from Southeast Asia into Alaska in a similar manner [*AMAP*, 2002]. In the summertime, the high and low pressure cells that govern wintertime Arctic pollution transport are less strong which decreases PAN transport.

Measurements of PAN mixing ratios indicate a seasonal cycle with maximum PAN levels in spring and minimum levels in late summer. *Beine and Krognes* [2000] report measurements of PAN in the European Arctic that show a seasonal cycle of PAN with a springtime maximum (mean value of 223 pptv) and a summer minimum (mean value of 92 pptv) from 1994 to 1996. The mean springtime mixing ratio of 223 pptv measured by *Beine and Krognes* [2000] can be compared with other Arctic PAN mixing ratios from *Bottenheim et al.* [1993] at Alert, Northwest Territories, Canada of 291 pptv recorded between March and April 1988 and 138 pptv at the Poker Flat Research Range, Alaska recorded between March and May 1993 [*Beine et al.*, 1996]. *Roberts et al.* [1998] report a mean PAN mixing ratio at Chebogue Point, Nova Scotia, Canada of 49 pptv for August to September 1993 which can be compared with the summertime mean value of 92 pptv from *Beine and Kronges* [2000]. This seasonal cycle is consistent with transport patterns and also thermal decomposition as discussed in the next section.

1.4 Decomposition

1.4.1 Thermal decomposition

The dominant destruction pathway of PAN in warmer locations is thermal decomposition, the reverse of reaction 1.3. Thermal decomposition is highly temperature

dependent as shown by PAN's high pressure limit Arrhenius rate expression, $k_{\infty(1.3rev)}$. The temperature dependence of PAN's lifetime due to thermal decomposition, assuming no recombination (reaction 1.3), is shown in figure 1.2. When the recombination reaction is taken into account, the lifetime of PAN is increased. The PAN recombination reaction's effect on thermal decomposition is confirmed by *Orlando et al.* [1992] who report an effective first order rate constant, k_b, (*i.e.* corrected for the recombination reaction) of 1.2×10^{-6} s^{-1} at 298 K in the presence of $\cdot NO_2$. At 298 K, the presence of the recombination reaction increases the atmospheric lifetime of PAN from approximately 45 minutes (predicted by $k_{\infty(1.3rev)}$) to approximately 9 days assuming initial PAN and $\cdot NO_2$ concentrations are nearly equal [*Orlando et al.*, 1992]. An irreversible loss in the PAN atmospheric reservoir occurs when $CH_3C(O)OO\cdot$ or $\cdot NO_2$ reacts with other molecules. A common reaction of the peroxyacetyl radical is with NO·,

$$CH_3C(O)OO\cdot + NO\cdot \rightarrow \cdot CH_3 + CO_2 + \cdot NO_2 \,. \qquad (1.4)$$

If $CH_3C(O)OO\cdot$ reacts with NO·, PAN is irreversibly lost. *Orlando et al.* [1992] shows that addition of reaction 1.4 leads to an effective thermal decomposition rate constant (k_b) that depends on the high pressure pure thermal decomposition rate constant ($k_{\infty(1.3rev)}$), the concentrations of ·NO and $\cdot NO_2$, the high pressure rate constants for recombination of PAN as shown in reaction 1.3 ($k_{\infty(1.3)}$) and reaction 1.4 ($k_{\infty(1.4)}$),

$$k_b = k_{\infty(1.3rev)} \frac{k_{\infty(1.4)}[\cdot NO]}{k_{\infty(1.3)}[\cdot NO_2] + k_{\infty(1.4)}[\cdot NO]}. \qquad (1.5)$$

Trost [2000] observed the effective thermal decomposition of PAN was approximately 8 times slower than pure PAN thermal decomposition for remote Northern Pacific marine air masses. Therefore, we see that actual loss of PAN *via* thermal decomposition depends on subsequent reactions and is highly dependent on actual environmental conditions.

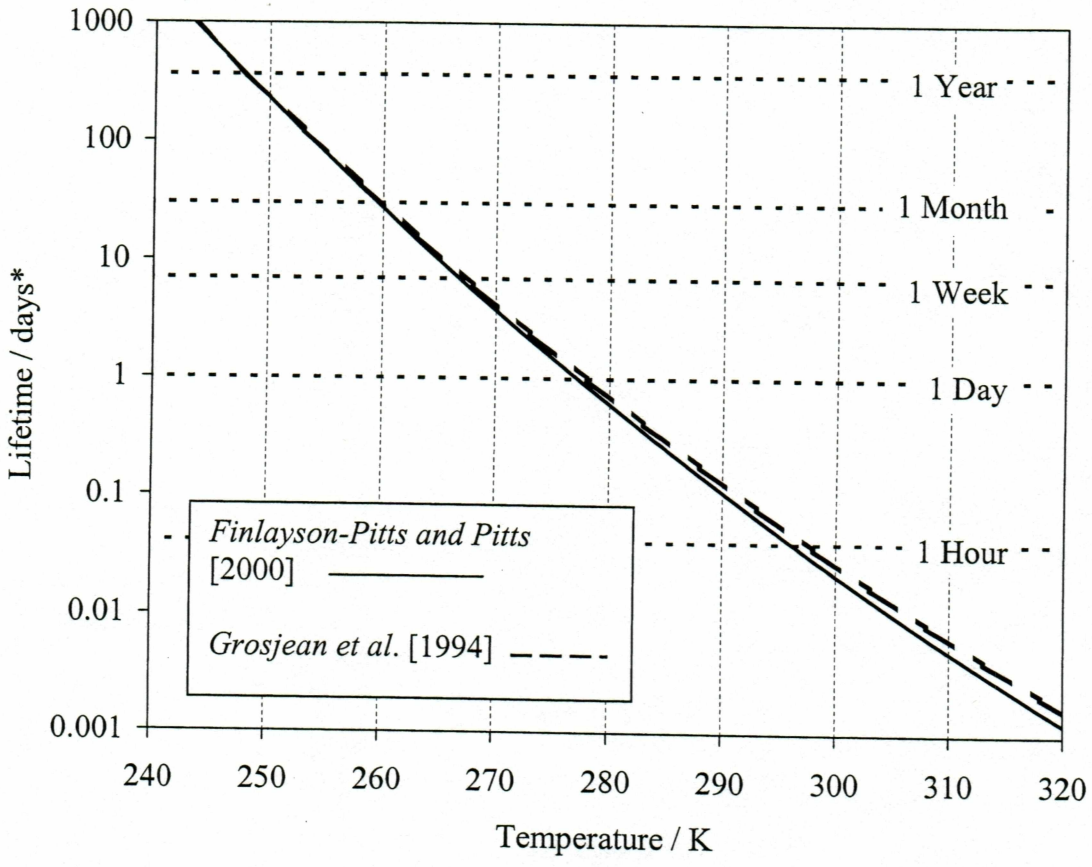

Figure 1.2 The lifetime of PAN due to thermal decomposition (*assuming no PAN recombination). The high pressure rate constant, $k_{\infty(1.3rev)} = 5.4 \times 10^{16} s^{-1} \exp(-13830\ K/T)$, from *Finlayson-Pitts and Pitts* [2000] was used in calculations. The R is the universal gas constant and T is temperature. *Grosjean et al.* [1994] report $k_{\infty(1.3rev)}$ is $1.58 \times 10^{16} s^{-1} \exp(-112.5 kJ / mol)/RT)$ and these values are plotted for comparison.

1.4.2 Reaction with the hydroxyl radical (·OH)

Another atmospheric sink for PAN is reaction with the hydroxyl radical (·OH). The main source for ·OH is ozone (O_3) photolysis producing an excited state oxygen atom, $O(^1D)$, which then reacts with H_2O vapor,

$$O_3 + h\nu \rightarrow O(^1D) + O_2 \quad (1.6)$$

$$O(^1D) + H_2O \rightarrow 2{\cdot}OH\,. \quad (1.7)$$

Peroxyacetyl nitrate reacts with ·OH,

$$PAN + {\cdot}OH \rightarrow \text{products}\,. \quad (1.8)$$

Talukdar et al. [1995] measured an upper limit of $< 3 \times 10^{-14}$ cm^3 $molecule^{-1}$ s^{-1} for the rate constant $k_{(1.8)}$. Assuming the globally averaged concentration for ·OH is 10^6 molecules cm^{-3} [*Prinn et al.*, 2001], the PAN lifetime with respect to reaction 1.8 is > 1 year. Therefore, the reaction between PAN and ·OH is slow and not likely the major atmospheric loss process for PAN.

1.4.3 Photolysis

At high altitudes in the troposphere or at high latitudes where colder temperatures exist, the thermal decomposition of PAN slows, increasing the importance of PAN photolysis. For example, at 0°F (-18°C) the pure thermal decomposition lifetime of PAN is approximately 77 days. The photolytic lifetime of PAN at the surface and at latitude 30°N according to *Talukdar et al.* [1995] is approximately 43 days. Therefore, it appears that photolysis is a faster sink of PAN than is thermal decomposition. Also, we have noted that the effective thermal decomposition lifetime may be longer than the pure thermal decomposition lifetime due to recombination. Thus, PAN photolysis needs to be further studied to understand its role in PAN decomposition.

Multiple products may be produced in PAN photolysis, some of which lead to irreversible loss while other products may recombine. Some possible PAN photolytic pathways are,

$$CH_3C(O)OONO_2 + h\nu \rightarrow CH_3C(O)OO\cdot + \cdot NO_2 \quad (1.9)$$

$$CH_3C(O)OONO_2 + h\nu \rightarrow CH_3C(O)\cdot + O_2 + \cdot NO_2 \quad (1.10)$$

$$CH_3C(O)OONO_2 + h\nu \rightarrow CH_3C(O)O\cdot + \cdot NO_3 . \quad (1.11)$$

The products of reaction 1.9 can recombine in a similar manner to the products of reaction 1.3. Reaction 1.10 can also lead to reformation of PAN *via* reaction 1.2 followed by reaction 1.3. In contrast, reaction 1.11 forms the nitrate radical ($\cdot NO_3$) which is rapidly photolyzed during the day and represents a true atmospheric sink for PAN. Additionally, the organic radical product of reaction 1.11 decomposes rapidly into CO_2 and $\cdot CH_3$ [*Bridier et al.*, 1991],

$$CH_3C(O)O\cdot \rightarrow CO_2 + \cdot CH_3 . \quad (1.12)$$

In addition to reactions 1.9 to 1.11, PAN can be photolyzed to form photoexcited $\cdot NO_3$ and $\cdot NO_2$ (represented by an asterisk *),

$$CH_3C(O)OONO_2 + h\nu \rightarrow CH_3C(O)OO\cdot + \cdot NO_2^* \quad (1.13)$$

$$CH_3C(O)OONO_2 + h\nu \rightarrow CH_3C(O)O\cdot + \cdot NO_3^* . \quad (1.14)$$

Nitric oxide ($\cdot NO$) can also be formed,

$$CH_3C(O)OONO_2 + h\nu \rightarrow CH_3C(O)OO\cdot + \cdot NO + O\cdot . \quad (1.15)$$

Figure 1.3 shows an energy diagram for PAN photolysis. The various energetic thresholds represent the possible photolytic pathways for PAN. The energy of $\cdot NO_2^*$ is based upon the approximate 590 nm cutoff of the strong absorption of the $\cdot NO_2$ band [*Finlayson-Pitts and Pitts*, 2000]. The energy of $\cdot NO_3^*$ formation is calculated from the vertical transition energy, 662 nm which equals 180.7 kJ/mol [*Finlayson-Pitts and Pitts*, 2000]. The energy required to dissociate to $\cdot NO_2$ into $NO\cdot$ and $O\cdot$ is 299.0 kJ/mol (400

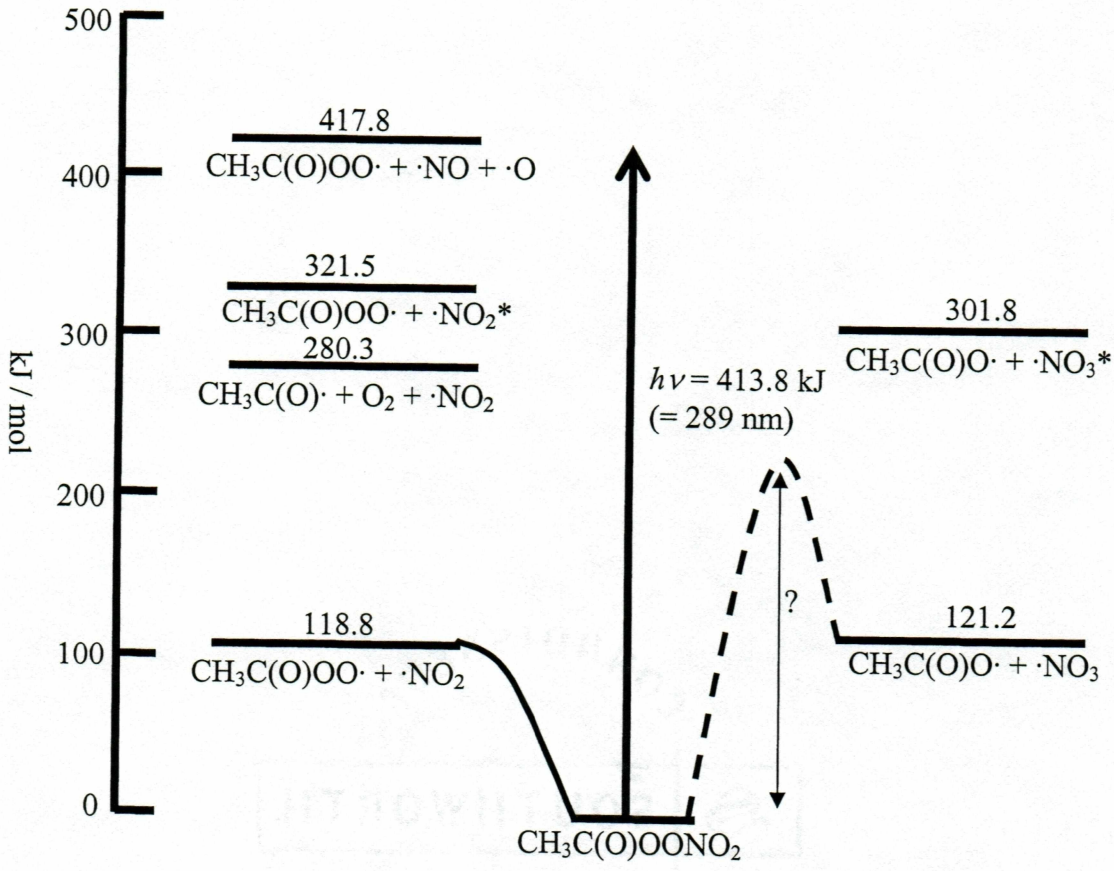

Figure 1.3 An energy diagram for the photodissociation of PAN. A discussion of the literature sources for the energetics of this diagram appears in the text.

nm threshold) [*Miller et al.*, 1999]. The energy required for $CH_3C(O)\cdot$ reacting with O_2 to form $CH_3C(O)OO\cdot$ is -161.5 kJ/mol [*DeMore et al.*, 1997]. The arrow represents the energy associated with a photolytic wavelength of 289 nm, which was used in this work on PAN photolysis.

Using laser induced fluorescence (LIF), *Mazely et al.* [1997] measured the branching ratio between the photoproducts of PAN ($\cdot NO_2$ and $\cdot NO_3$). The branching ratio for the photolytic pathways is called the quantum yield (ϕ). The quantum yield for formation of a specific product is defined as the number of specific photoproducts divided by the total number of excited molecules. *Mazely et al.*[1997] measured $\phi_{NO_3} = 0.3 \pm 0.1$ and $\phi_{NO_2} = 0.83 \pm 0.09$ for PAN at a photolytic wavelength, λ, of 248 nm with pressures ranging from 0.1 Torr to 20 Torr. These results indicate that $\cdot NO_2$ and $\cdot NO_3$ are the only nitrogen containing photoproducts of PAN at 248 nm because the sum of these quantum yields is within error of 1. Recently, *Harwood et al.* [2003] determined $\phi_{NO_3} = 0.19 \pm 0.04$ and 0.41 ± 0.10 at 248 and 308 nm respectively. The quantum yield values from *Harwood et al.* [2003] show a possible dependence on wavelength because there is an approximate doubling of the amount of $\cdot NO_3$ formed between wavelengths from 248 nm to 308 nm. Thus, a ϕ_{NO_3} wavelength dependent study is needed.

At higher pressures, which are typical in the atmosphere, PAN may be photoexcited by absorbing a photon and may undergo deactivation by colliding with another molecule in the atmosphere. This process is known as molecular quenching and follows the reaction sequence

$$CH_3C(O)OONO_2 + h\nu \rightarrow CH_3C(O)OONO_2^* \quad (1.16)$$

$$CH_3C(O)OONO_2^* + M \rightarrow CH_3C(O)OONO_2 + M^*, \quad (1.17)$$

where $CH_3C(O)OONO_2^*$ is an excited PAN molecule and M is a molecule that collides and receives energy from the excited PAN molecule. Molecular quenching may affect

quantum yields, thus pressure dependent studies should be performed to determine if quenching is important in PAN's atmospheric chemistry.

The goal of this research was to determine the importance of photolysis of PAN producing $\cdot NO_3$ *via* reaction 1.11 and determine the dependence of this reaction on photolysis wavelength. An ultra sensitive detection technique called cavity ring-down spectroscopy (CRDS, described in section 3.2) was used which allowed detection of $\cdot NO_3$ in previously undetectable concentrations. Cavity ring-down spectroscopy may also be used to determine pressure dependence of the $\cdot NO_3$ quantum yield because CRDS is independent of sample pressure.

Chapter 2

Synthesis and photochemical properties of PAN and dinitrogen pentoxide (N_2O_5)

2.1 Introduction

This chapter provides a detailed description of PAN synthesis and data from the literature on PAN photochemical properties. These photochemical properties are the absorption cross sections in the infrared (IR) and the ultraviolet (UV) spectral regions. Quantification of the PAN concentration delivered to the vacuum chamber during the photolysis experiment used IR spectroscopy. The UV absorption cross section is used to calculate the number of photoexcited PAN molecules. Dinitrogen pentoxide (N_2O_5), which also yields $\cdot NO_3$ from photolysis, was used as a reference molecule for the $\cdot NO_3$ quantum yield from PAN photolysis determination and its photochemical properties are discussed in this chapter.

2.2 Synthesis of PAN

Peroxyacetyl nitrate (PAN) was synthesized by nitration of peracetic acid [*Gaffney et al.*, 1984]. The PAN sample was prepared by adding 25 mL of n-tridecane (Aldrich, 99% pure) to a 50 mL round bottom flask equipped with a magnetic stirrer. The n-tridecane was cooled for 5 minutes in a salt-ice bath to approximately 0°C. Precisely 2.5 mL of peracetic acid (Aldrich, 32 % weight in a mixture of acetic acid, hydrogen peroxide and water) was added to the cooled n-tridecane. Next, 2.0 mL of concentrated H_2SO_4 was added to the mixture and stirred for 5 minutes. After 5 minutes and while the mixture was still in the salt-ice bath, 0.5 mL of nitric acid was added drop-wise to the mixture which was cooled for another 5 minutes. The n-tridecane layer was then poured onto 25 mL of cooled water (high-performance liquid chromatography (HPLC) grade) in a separation funnel. The n-tridecane layer was washed a second time

and the PAN/n-tridecane mixture was poured into a glass trap. The PAN/n-tridecane mixture was stored frozen at -40°C in an ultra cold freezer.

2.3 Photochemical properties of PAN

Quantitative IR spectroscopy was used to determine the PAN concentration being delivered to the photolysis chamber. For this purpose, the absorption strength of PAN's absorption peaks needs to be known. A sample IR spectrum is shown in figure 2.1. Strong PAN absorbance peaks are present at 1841, 1740, 1302, and 1163 cm^{-1} [*Gaffney et al.*, 1984]. Table 2.1 shows integrated band strengths, S, for PAN in atm^{-1} cm^{-2} using base 10 absorption units measured by *Gaffney et al.* [1984]. These integrated band strengths were converted into IR absorption band strengths, S', in cm^2 $molecule^{-1}$ cm^{-1} using the reported values for the integrated band strengths at the observed temperature, 298 K [*Gaffney private communication*]. For infrared spectroscopic analysis, all IR absorption strengths (represented by either S and S' for PAN and ε for N_2O_5) listed in this thesis are base 10.

Ultraviolet (UV) absorption cross sections, σ, in cm^2 $molecule^{-1}$ base e absorption units have been measured by *Talukdar et al.* [1995]. Base e absorption units are used for all UV absorption cross sections (represented by σ) in this thesis. Peroxyacetyl nitrate UV absorption cross sections are plotted with N_2O_5 UV absorption cross sections in figure 2.2 to show the differences in absorption cross section between the two molecules with respect to wavelength. As shown, the PAN molecule has a smaller UV absorption cross section than N_2O_5. The N_2O_5 UV absorption cross sections in figure 2.2 are discussed in the next section.

2.4 Photochemical Properties of N_2O_5

The IR absorption spectrum for N_2O_5, shown in figure 2.3, shows distinct absorption peaks for N_2O_5 at 1246 and 1720 cm^{-1} [*Wangberg et al.*, 1997]. If present, $\cdot NO_2$ would

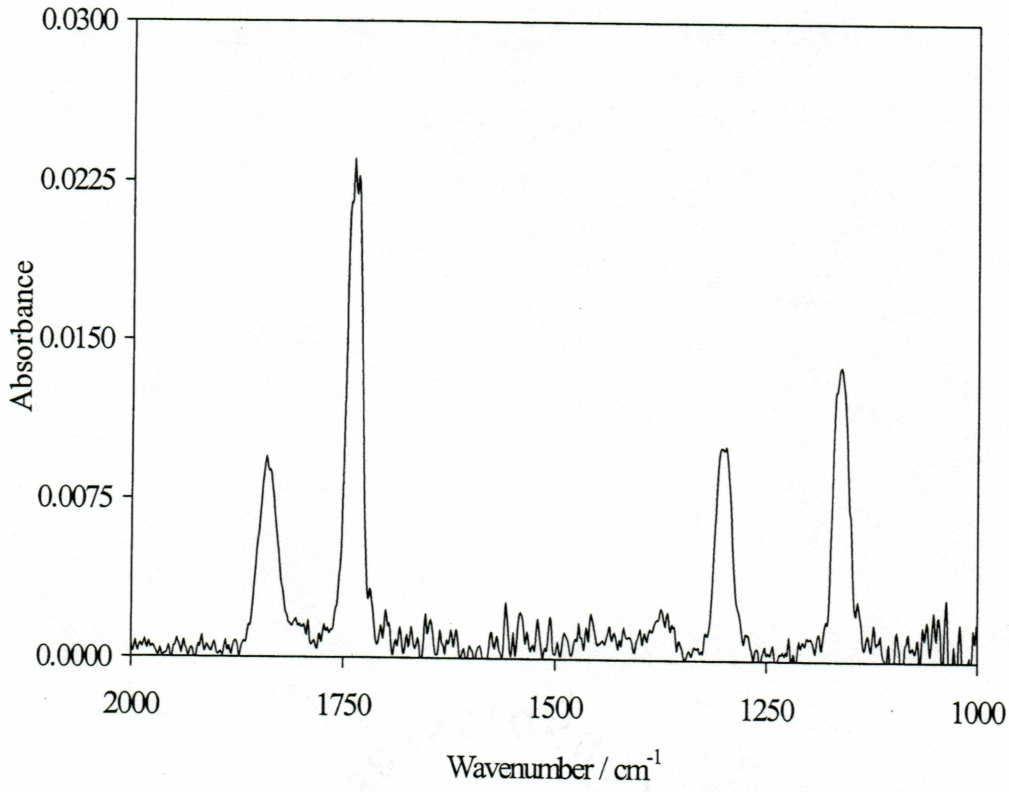

Figure 2.1 An infrared spectrum of PAN. The resolution is 4.0 cm^{-1}. Peroxyacetyl nitrate peaks are at 1841, 1741, 1302, and 1163 cm^{-1}.

Table 2.1 Infrared integrated band strengths, S (base 10), and converted band strengths, S' (base 10), for PAN. All integrated band strengths S were taken from *Gaffney et al.* [1984] and were converted assuming S was measured at 298 K. See text for discussion.

Wavenumber / cm^{-1}	S / atm^{-1} cm^{-2}	S' / 10^{-17} cm^2 $molecule^{-1}$ cm^{-1}
1841	322	1.31
1741	808	3.28
1302	405	1.65
1163	477	1.94

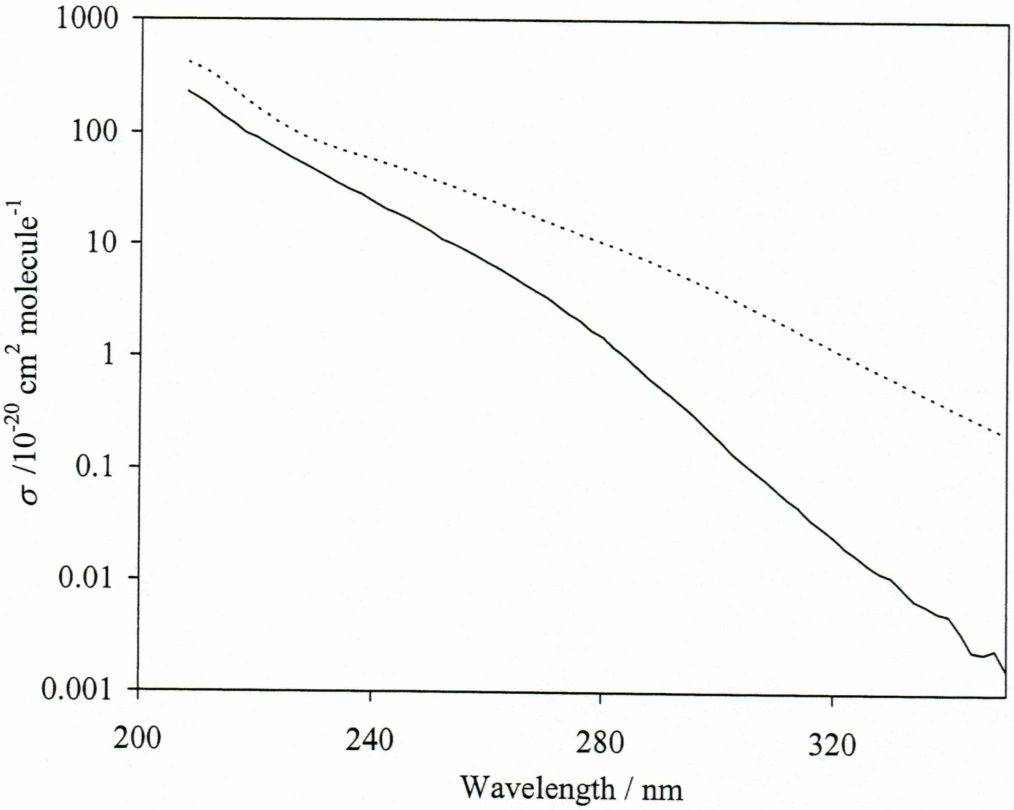

Figure 2.2 The ultraviolet absorption cross sections, σ (base e), for N_2O_5 and PAN at 300 K. The dashed line represents N_2O_5 and the solid line represents PAN. These σ values are from *DeMore et al.* [1997].

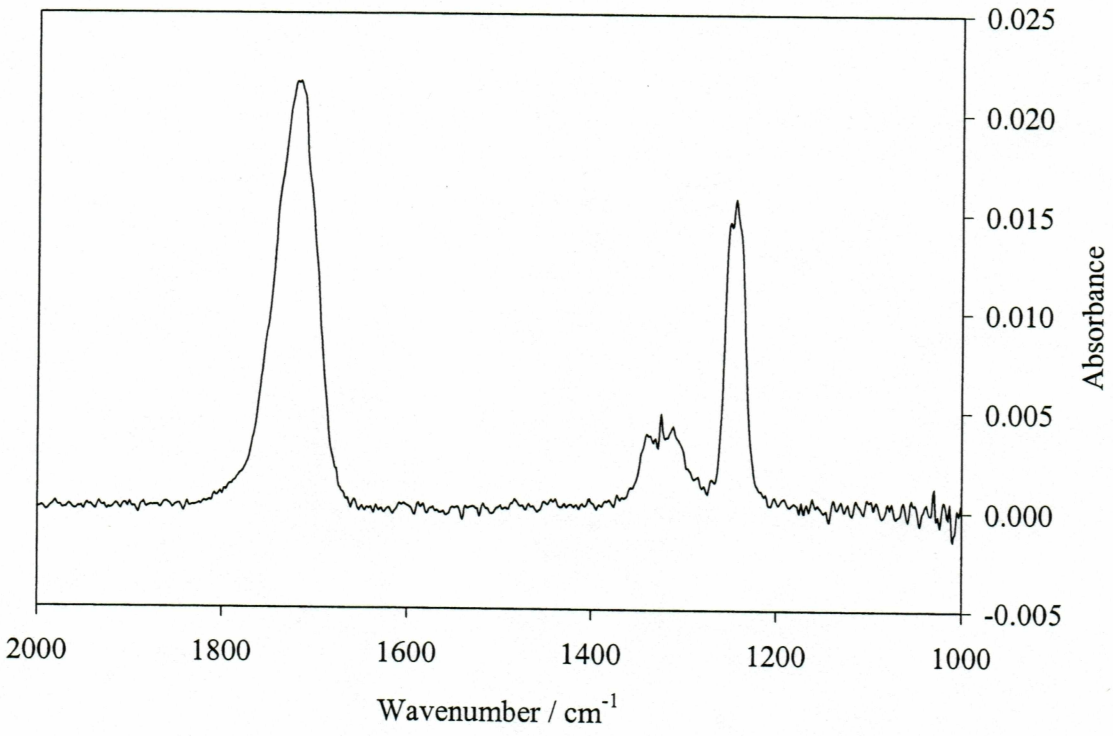

Figure 2.3 An infrared spectrum of N_2O_5. The resolution is 4.0 cm^{-1}. The absorption peaks of N_2O_5 are at 1246 and 1720 cm^{-1}. The absorption peak at 1326 cm^{-1} is due to nitric acid (HNO_3) contamination.

be observed at 1600 cm^{-1} [*Finlayson-Pitts and Pitts*, 2000]. The structured absorption at 1326 cm^{-1} is nitric acid (HNO_3) contamination. The IR peak absorption cross section, ε, from *Wangberg et al.* [1997], for N_2O_5 at 1246 cm^{-1} is 8.56 x 10^{-19} cm^2 $molecule^{-1}$. The N_2O_5 peak at 1720 cm^{-1} was not used to quantify the number density of N_2O_5 because HNO_3 absorbs near the same wavenumber.

The UV absorption cross sections, σ, for N_2O_5 at 300 K displayed in figure 2.2 are the absorption cross sections from *DeMore et al.* [1997]. As shown in figure 2.2, the UV absorption cross sections for N_2O_5 are larger than those for PAN. Therefore, more UV light is absorbed by N_2O_5 than PAN. This increases the amount of N_2O_5 photoproduct ($\cdot NO_3$) with respect to PAN, assuming nearly equal concentrations of N_2O_5 and PAN are used.

The photolysis of N_2O_5 has been studied by *Ravishankara et al.* [1986] and *Swanson et al.* [1984]. The most likely photolytic pathways are

$$N_2O_5 + h\nu \rightarrow \cdot NO_3 + \cdot NO_2 \qquad (2.1)$$

$$N_2O_5 + h\nu \rightarrow \cdot NO_3 + \cdot NO + O(^3P)\,. \qquad (2.2)$$

Both reactions form $\cdot NO_3$ and *Ravishankara et al.* [1986] report a value near unity for the quantum yield of $\cdot NO_3$ at 248 nm. Recently, *Harwood et al.* [2003] reported a value of 0.8 for the $\cdot NO_3$ quantum yield from N_2O_5 photolysis at 248 nm. However, *DeMore et al.* [1997] recommends 1.0 for the $\cdot NO_3$ quantum yield from N_2O_5 at 289 nm. This work uses 1.0 for the $\cdot NO_3$ quantum yield from N_2O_5 at 289 nm.

Chapter 3
Experimental and system design

3.1 Introduction

A unique system was built for $\cdot NO_3$ quantum yield from PAN photolysis determination. In this system, photolytic precursors of $\cdot NO_3$, N_2O_5 or PAN, could be rapidly switched, allowing the relative amount of $\cdot NO_3$ formed *via* photolysis to be determined. The precursors flowed into an IR cell where the number density of N_2O_5 or PAN was determined by Fourier transform infrared spectroscopy (FTIR). The precursors were then delivered into a vacuum chamber. The geometry and flow design of the vacuum chamber are discussed in this chapter. We then photolyzed the precursors inside the vacuum chamber using a tunable frequency-doubled dye laser. A second dye laser probed the $\cdot NO_3$ photoproduct using a highly sensitive absorption technique called cavity ring-down spectroscopy (CRDS). Because CRDS detection is central to our experiment, we initially review its principles then describe how we integrate CRDS detection into the experimental system.

3.2 Overview of cavity ring-down spectroscopy (CRDS)

Cavity ring-down spectroscopy (CRDS) is a highly sensitive absorption technique that allows detection of $\cdot NO_3$ at number densities as low as 10^7 molecules cm^{-3} (0.4 pptv at 1 atm, 298 K) [*Simpson*, 2003]. Cavity ring-down spectroscopy has been reviewed by *Busch and Busch* [1999] and *Dick* [2002]. This section briefly describes the basic principles behind CRDS.

Figure 3.1 shows a schematic diagram of the CRDS system. The ring-down cavity is made of two highly reflective mirrors facing each other. The CRDS system uses a pulsed neodynium^{3+} yttrium-aluminum garnet (Nd:YAG) laser (Quanta Ray: LAB-150-10) that emits fundamental radiation at 1064 nm. This light is frequency doubled to 532 nm

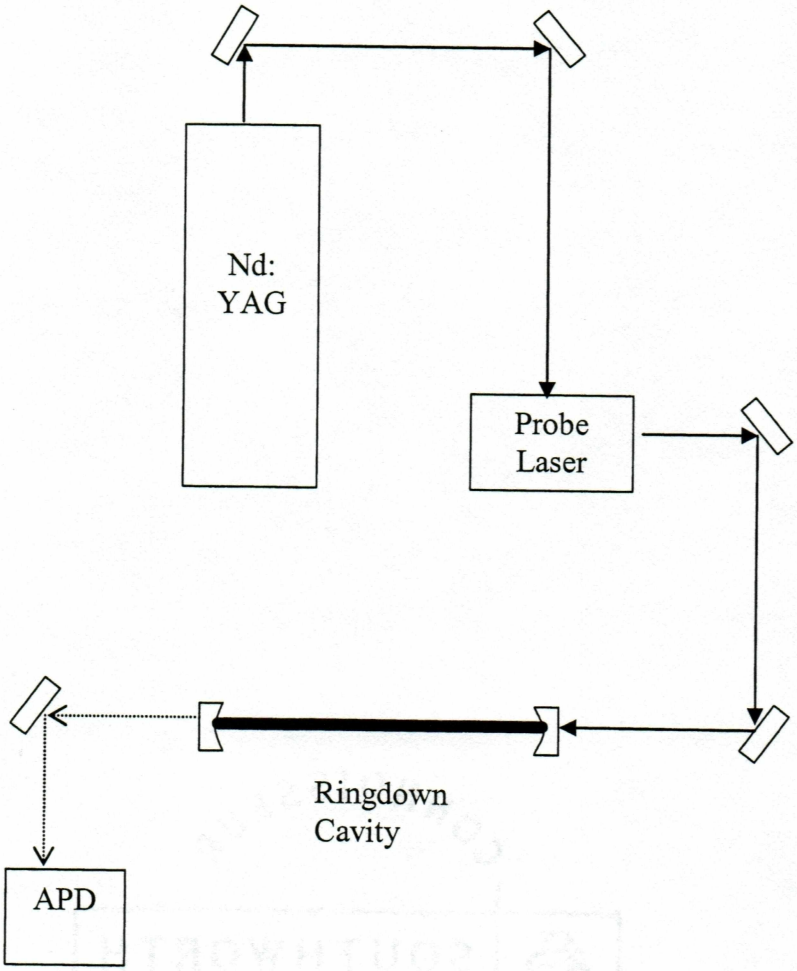

Figure 3.1 A block diagram of the CRDS setup. Fixed wavelength light from the Nd:YAG laser is directed into a probe laser. Light from the probe laser is then directed into the ring-down cavity and leaks from the backside of the mirror opposite the source. An avalanche photodiode detector (APD) detects the light signal.

which pumps a dye laser (Dakota Technologies: Northern Lights). The tunable light emitted from the dye laser acts as a light source for the CRDS absorption measurements. The probe laser fires laser pulses at 10 sec^{-1} (Hz). These pulses are directed onto the back of the cavity input mirror, and a tiny fraction of the pulse transmits through the mirror. This light is trapped within the cavity by being reflected back and forth between two highly reflective mirrors. The high reflectivity of the mirrors allows the instrument to achieve long effective pathlengths (on the order of 9 km). The light that builds up within the cavity eventually decays due to imperfect mirror reflectivity and molecular absorption by the gas sample. The loss due to imperfect mirror reflectivity is typically greater than that due to molecular absorption. This mirror loss causes the light signal within the cavity to exponentially "ring down". The light intensity leaking out of the cavity is measured behind the output mirror on the opposite side from the light source with an avalanche photodiode detector (APD) (Hamamatsu: C5460). The detector converts the light signal into an electronic signal measured in Volts (V). The exponential light signal decay fits,

$$I(t) = I_0 e^{-t/\tau}. \tag{3.1}$$

The observed light intensity as a function of time t is $I(t)$ and I_0 is the initial light intensity. The time it takes for the signal to decay to $1/e$ of its initial value is the ring-down time, τ. The exponential light intensity decay is fitted with LabVIEW software using a weighted linear least-squares fit analysis. The threshold value triggering detection is 3 V and all data over 9 V are ignored because of saturation. The fit result is the ring-down time. The ring-down time is converted into a loss rate, r, by,

$$r = (c\tau)^{-1}, \tag{3.2}.$$

where the loss rate, r, describes the loss of light per distance and is the sum of all light losses and c is the speed of light. The loss rate can be used to determine a molecular

number density using a modified form of Beer's Law ($A = N\sigma l$). In Beer's Law, A is the absorbance, N is the number density, σ is the absorption cross section, and l is the pathlength. The absorption per distance, r_{abs}, is,

$$r_{abs} = \frac{A}{l} = \frac{N\sigma l}{l} = N\sigma . \tag{3.3}$$

The loss rate, r, equals an empty cavity loss rate (called the baseline loss rate, r_{BL}) plus any molecular absorption by a gas in the cavity,

$$r = r_{BL} + r_{abs} . \tag{3.4}$$

A change in the loss rate, Δr, is determined by subtracting the absorbing loss rate from the baseline loss rate,

$$\Delta r = \frac{1}{c\tau} - \frac{1}{c\tau_{BL}} = r_{BL} + N\sigma - r_{BL} = N\sigma . \tag{3.5}$$

In equation 3.5, τ is the ring-down time with a molecular absorption and τ_{BL} is the baseline ring-down time. Using CRDS and equation 3.5, we can determine the number density of $\cdot NO_3$ formed in PAN and N_2O_5 photolysis. To convert these results into a quantum yield, we also need to know the number density of the photolytic precursors.

3.3 Precursor generation and number density determination using IR spectroscopy

For the relative quantum yield determination, the experimental setup was adapted to switch flows between PAN and N_2O_5 precursor gases. The experimental setup depicted in figure 3.2 includes the equipment necessary to switch flows between the precursors. This switching flow setup allowed us to change between N_2O_5 and PAN rapidly while keeping the same experimental conditions for both of the precursors' photolysis experiments. For PAN number density determination, IR spectroscopy was used. The previously frozen PAN/n-tridecane mixture was defrosted and kept in an ethylene glycol (EG)/water bath at -2 °C. The N_2 carrier gas (ultra-high purity (UHP) grade) at a flow rate of 100 standard $cm^3\ min^{-1}$ (sccm) "blew" on the surface of the PAN/n-tridecane

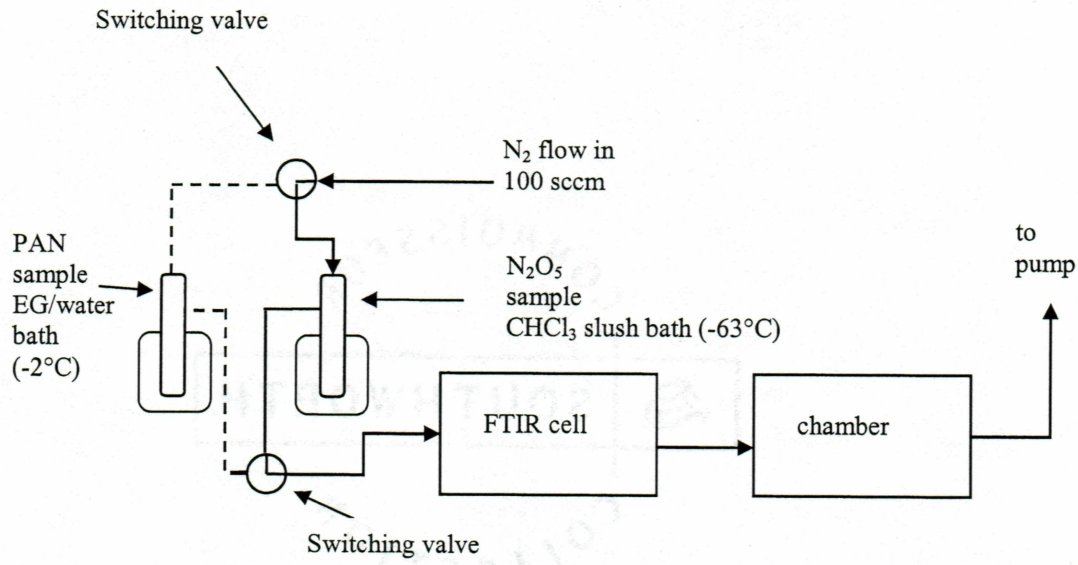

Figure 3.2 A block diagram for the switching precursor flows. The N_2 main flow is 100 sccm and can switch between the N_2O_5 sample and the PAN/tridecane mixture. The switching valves in this diagram depict N_2O_5 being delivered to the chamber.

picking up PAN vapor. The PAN vapor present in the carrier gas flowed into an IR gas cell 17 cm long with calcium fluoride (CaF_2) windows. The CaF_2 windows allowed detection of the PAN absorption peaks in the IR spectral range and are less hygroscopic than most other IR windows. For PAN number density determination, an IR spectrum of PAN was recorded using a Fourier transform infrared spectrometer (Perkin Elmer Paragon 1000) at 4.0 cm^{-1} resolution. This PAN flow system delivered sufficient quantities of PAN into the IR gas cell although the PAN concentration slowly decreased over a short time period (about 1 hour).

The N_2O_5 used in the experiment had been previously synthesized according to the method described in *King et al.* [2000] was and stored frozen in a glass trap at -40°C in an ultra-cold freezer. To deliver N_2O_5, a flow rate of 100 sccm N_2 carrier gas (UHP grade) flowed into the N_2O_5 glass trap kept in a chloroform ($CHCl_3$) slush bath at -63 °C. The same FTIR method for PAN number density determination was used for N_2O_5 number density determination.

3.4 System design

3.4.1 Vacuum chamber design

The vacuum chamber was made of 3" outer diameter (OD) stainless steel tubing with the inlet connected to ½" OD, 3/8" inner diameter (ID), Teflon™ tubing. Stainless-steel 1½" OD sidearms were located in the middle of the main chamber at a 30° crossing angle. Flexible polyethylene tubing (Tigerflex™) connected the vacuum chamber to a two-stage mechanical vacuum pump (Edwards E2M18) that evacuated the chamber. The vacuum chamber was equipped with a top flange with a ½" OD fitting (Ultratorr) for a pressure gauge (MKS Type 622) that monitored the pressure inside the chamber. Typical pressures used for the experiments were 10 - 760 Torr.

A leak rate was determined to insure that the sample was not contaminated through system leaks. The gas leak rate for the vacuum chamber was determined by timing the leak rate, L, in atm min^{-1}. This rate was measured by recording the increase in pressure with respect to time while the vacuum chamber was evacuated but the vacuum was not pumping. The volume of the vacuum chamber, V, in cm^3 was multiplied by L to give the leak rate for the vacuum chamber in atm cm^3 min^{-1}, which are equal to sccm ($L(V)$ = leak rate in sccm). The measured leak rate was 0.1 – 0.2 sccm, which was small compared to a total system flow of 100 - 1000 sccm.

To insure N_2O_5 was not lost on the chamber surface, we measured the N_2O_5 number density before and after the chamber using IR spectroscopy. A schematic of the flow system setup for the surface loss chamber test is shown in figure 3.3. In this setup, the order of flow through the IR cell and chamber could be reversed, allowing measurement of N_2O_5 number density before and after the chamber. The pressure of the system was approximately 10 Torr and the N_2 carrier flow in the system was 100 sccm. The N_2O_5 was added to the N_2 flow by picking up N_2O_5 vapor at -63 °C (the temperature of the $CHCl_3$ slush bath). The flow direction was switched between before and after the vacuum chamber every 3 minutes to allow N_2O_5 number density determinations. The system was allowed to purge any N_2O_5 in the system between flow shifts for about 2 minutes. The number densities were converted into mixing ratios using measured pressures in the IR cell and the vacuum chamber. The average mixing ratios for the two flow directions were compared to determine the amount of N_2O_5 lost onto the surface of the stainless steel chamber. The N_2O_5 mixing ratios with the flow into the chamber first was within 98% ± 2% of the N_2O_5 mixing ratios flowing in the opposite direction. These data show that vacuum chamber wall loss for N_2O_5 was minimal. Because PAN is less sticky than N_2O_5 on stainless steel surfaces, the loss of PAN to the chamber surface

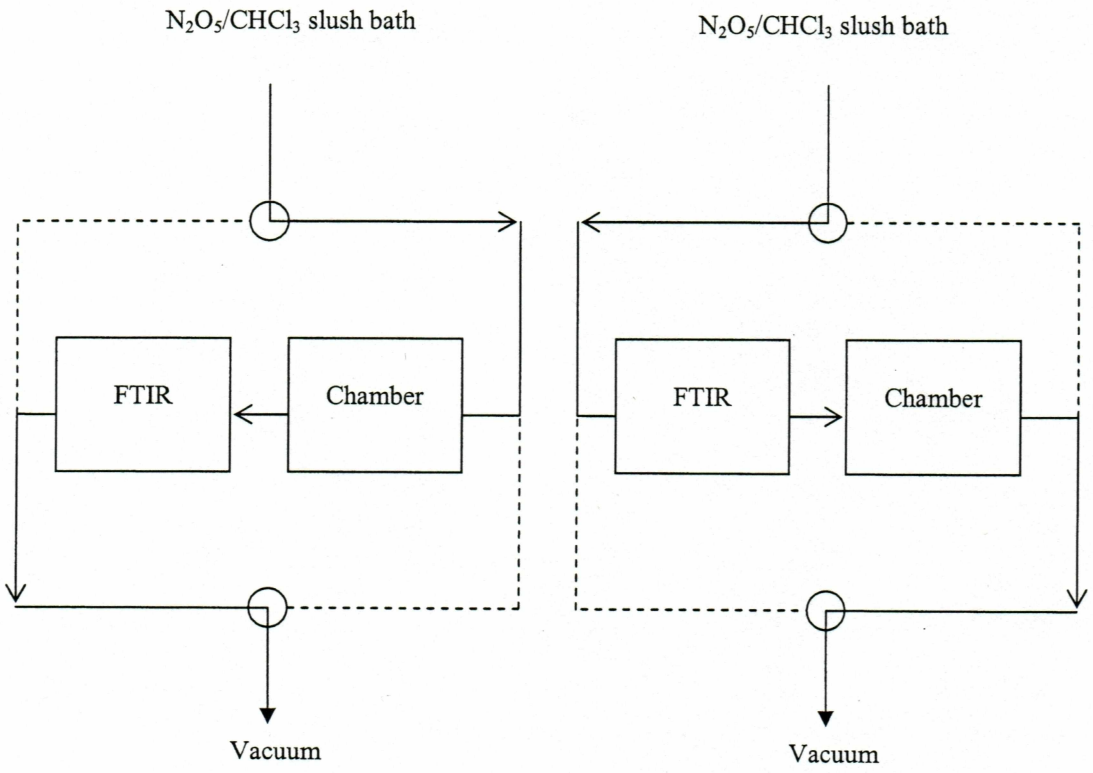

Figure 3.3 A block diagram of the switching flow system for surface loss test. The main flow of the system was 100 sccm. The pressure of the system was approximately 10 Torr. The flow direction switched every 3 minutes and purged for approximately 2 minutes before number density determination.

should be less than that of N_2O_5.

3.4.2 Purge flow design

The flow system in the vacuum chamber consisted of a main flow down the 3" main tube and a purge flow in the 1 1/2" sidearms. An added purge flow kept the CRDS mirrors clean and flushed any unwanted gases out of the sidearms. The sidearms on the vacuum chamber contained inlets for the N_2 purge gas and Teflon™ inserts to keep the main flow in the center of the chamber.

To determine if the flow system functioned properly, a water vapor spectrum in the visible light region was recorded and compared with a simulated water spectrum at a determined water mixing ratio. The mixing ratio of water present in the room air was obtained by attaching a Vaisala relative humidity gauge and a thermocouple onto the inlet of the vacuum chamber while recording an experimental water vapor spectrum. Room air flowed through the chamber at 400 sccm while 100 sccm N_2 purge gas flowed into the sidearms. A spectrum of water was recorded from 656 nm to 659 nm.

For the simulated water spectrum, the mixing ratio of water was converted into a water concentration at the determined temperature. The water concentration determined at the inlet to the vacuum chamber was corrected for the diluting N_2 purge flows in the center of the chamber. The main flow through the chamber was diluted by the sidearm purge flow that was closest to the inlet on the cavity due to the 30° angle. The other sidearm purge flow did not dilute the water sample. Because water absorption is directly proportional to water concentration, the simulated water absorption was multiplied by a dilution factor determined by,

$$A_{corrected} = A_{water} \frac{F_{main}}{0.5F_{purge} + F_{main}}. \qquad (3.6)$$

In equation 3.6, $A_{corrected}$ is the corrected absorption value for the simulated water spectrum, A_{water} is the simulated absorption value for water without the dilution correction, F_{purge} is the purge flow rate and F_{main} is the main flow rate.

The simulated water spectrum assumed a completely filled cavity between the ring-down mirrors. However, water absorption took place only in the water absorption pathlength, l_w, located in the center of the cavity. Therefore, the simulated water spectrum absorption was divided by a factor, l/l_w, where l is the mirror-to-mirror length. To determine l_w, the ID of the main chamber, d, was measured and divided by sin 30° to account for the 30° crossing angle between the sidearms and the main chamber (d/sin 30° = l_w). For the vacuum chamber, l_w is 14.5 cm. The mirror-to-mirror cavity length is 50 cm.

The spectrum derived from the computer simulation program was convoluted with a 1.1 cm^{-1} full-width half maximum Gaussian resolution (FWHM) to represent the probe laser bandwidth. The probe laser was specified to have a bandwidth of 1.0 cm^{-1} FWHM, but a better fit was obtained using 1.1 cm^{-1} FWHM. Figure 3.4 shows the comparison between the experimental water spectrum and the corrected simulated water spectrum. The standard deviation between the absorption peak heights is 14% (1σ) and 0.6% (1σ) for the peak widths. This verified that the purge flow and the Teflon™ inserts kept the sidearms clear of any unwanted gases. Also, this experiment determined that main chamber filled properly.

The flow in the main chamber during the photolysis experiment had to flush out the previously photolyzed precursor to insure that a fresh sample can be photolyzed every laser shot. To ensure that the linear flow rate is high enough to replenish a fresh sample, the photolysis experiments require that the length the flowing sample moves between

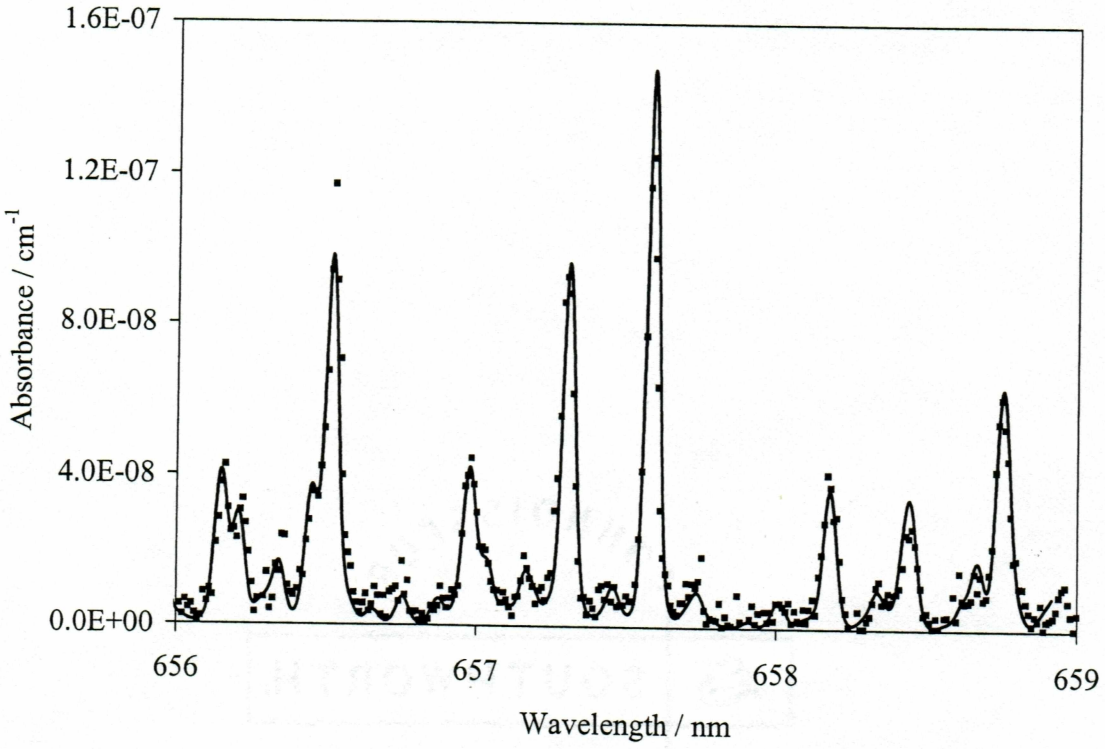

Figure 3.4 A comparison between an experimental water spectrum and a simulated water spectrum. The square points represent the experimental water spectrum and the line represents the simulated water spectrum with a convoluted resolution of 1.1 cm^{-1}. The standard deviation (1σ) in peak heights and widths is 14% and 0.6% respectively.

laser shots is greater than the laser beam width along the flow axis. The distance the sample moved per laser shot, l_F, is

$$l_F = \frac{F_l}{R}, \tag{3.7}$$

where F_l is the linear flow rate and R is the laser repetition frequency. The linear flow rate is given by,

$$F_l = \frac{F}{A}, \tag{3.8}$$

where F is the volumetric flow rate and A is the vacuum chamber cross-sectional area (41.7 cm^2). The volumetric flow rate is different from the standard flow rate because the chamber pressure is typically less than standard pressure (1 atm). Because a standard $cm^3\ min^{-1}$ actually equals atm $cm^3\ min^{-1}$, F is determined by,

$$F = \frac{0.5F_{purge} + F_{main}}{p}, \tag{3.9}$$

where p is the vacuum chamber pressure.

Table 3.1 shows combinations of commonly used flows and their shot-to-shot linear flow distance, l_F. In our case, the photolysis beam width is approximately 0.3 cm. Therefore, all these conditions satisfy the fresh sample requirement.

3.4.3 Photolysis system design

For the photolysis of PAN and N_2O_5, the Nd:YAG laser pumped another tunable dye laser equipped with a frequency doubling unit (Sirah: Cobra Stretch series) to produce tunable UV light 280 - 320 nm. A block diagram of the photolysis system is shown in figure 3.5. The power of the UV light was kept at 1 mJ for the photolysis experiments. The UV light passed through a shutter that allowed 5 laser pulses through the shutter then blocked the next 5 pulses. Next, the UV light passed through UV anti-reflective coated windows into the vacuum chamber. Figure 3.6 shows the paths of the beams in the crossing region. By design, the photolysis beam passed by the edge of each cavity ring-

Table 3.1 Combinations of commonly used flows and their shot-to-shot linear flow distance.

R / Hz	p / Torr	F_{main} / sccm	F_{purge} / sccm	l_F / cm
10	10	100	100	0.46
10	20	200	100	0.38
10	40	400	100	0.34
1	300	1000	200	1.11

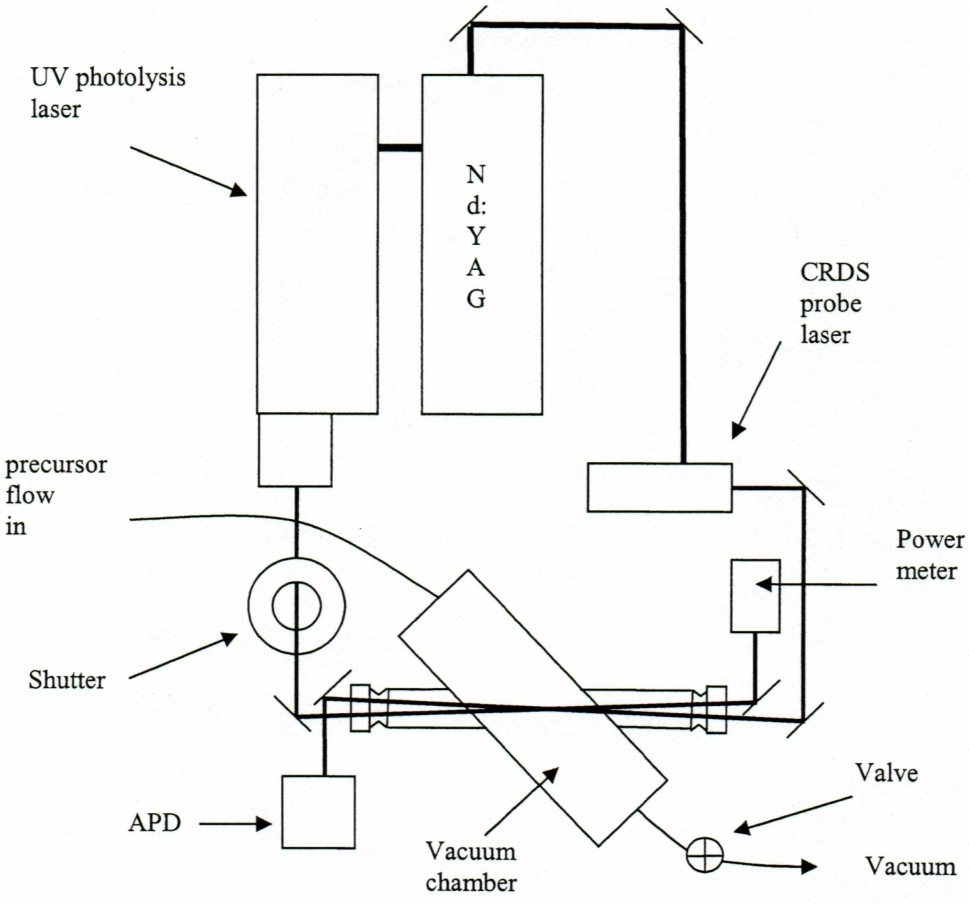

Figure 3.5 A block diagram for the photolysis system. The laser beams cross in the center of the vacuum chamber. The APD detects the ring-down signal and the power meter monitors the UV photolysis beam. Mirrors on the end flanges are adjusted with manipulators to optimize ring-down signal. Flexible bellows allow mechanical adjustment while maintaining a vacuum seal on the chamber.

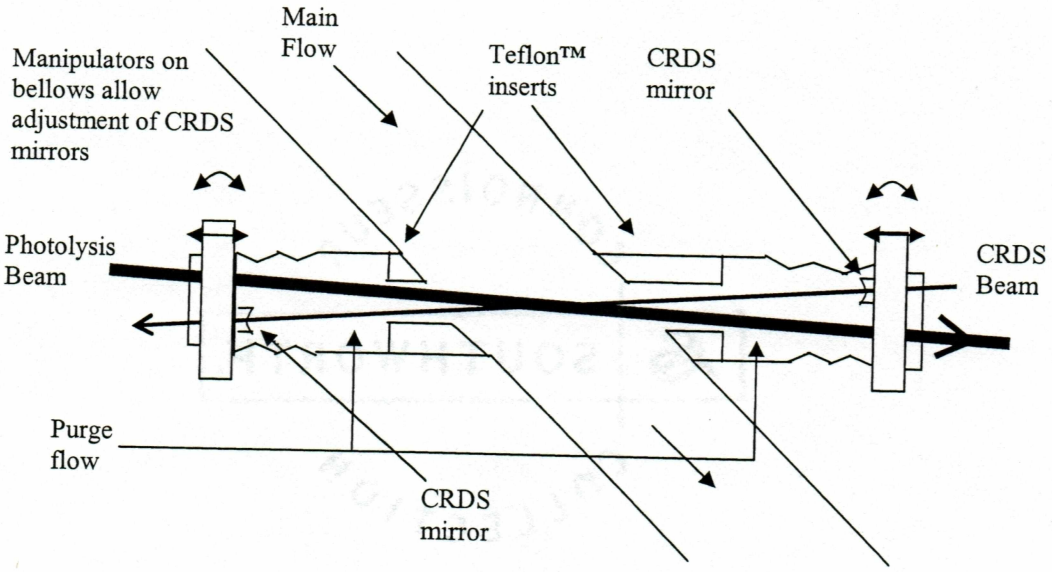

Figure 3.6 A schematic of the photolytic crossing region inside the vacuum chamber. The manipulators and flexible steel bellows allow horizontal and vertical adjustment of the CRDS mirrors. The photolysis beam passes by the edge of the CRDS mirrors. The CRDS mirrors are held into the sidearm flange that allows a mechanically solid mounting surface.

down mirror. The UV light crossed the probe laser beam to photolyze the molecule and the $\cdot NO_3$ photoproduct was detected by the CRDS probe laser.

The cavity ring-down mirrors were secured in the chamber by holders that overlapped the edge of the mirror and were screwed into the end sidearm flanges. The flanges provided a mechanically solid mounting surface. The vacuum seal was maintained by using flexible metal bellows coupler. Attached to each flange were manipulators that allowed the CRDS mirrors to move. These manipulators were adjusted to align the ring-down cavity for signal optimization. The UV beam and the probe laser beam heights were adjusted to cross at the same height and at the smallest possible angle.

When we began working with the system, we noticed that the photolysis beam caused the ring-down time to decrease even with an evacuated vacuum chamber. This sharp decrease in ring-down signal was attributed to UV light reflecting off the windows onto the CRDS mirrors causing a decrease in mirror reflectivity. We believe that mirror heating caused this degradation in ring-down time. If we blocked the UV beam, the mirrors regained their reflectivity on an approximate 10 min timescale, consistent with mirror cooling. The CRDS mirrors were made with a coating (Ta_2O_5) that absorbs UV light (*Research Electro-optics, private communication*) providing a mechanism for the UV heating effect. To decrease this effect, windows with < 0.05 % UV reflectivity were added and the CRDS mirror reflectivity decrease was minimized. Figure 3.7 shows a time-series of 5 UV shots on and 5 UV shots off averaged ring-down time measurements of an empty cavity. Measurements in on and off states are shown as different symbols. Clearly the mirror reflectivity decreases over the approximate 10 min timescale due to the UV effect. However, the difference between on and off data is small. The timescale of on and off switching (0.5 sec on then 0.5 sec off) is small enough to have little accumulated UV effect between the two states. The change in loss rate, Δr, between the

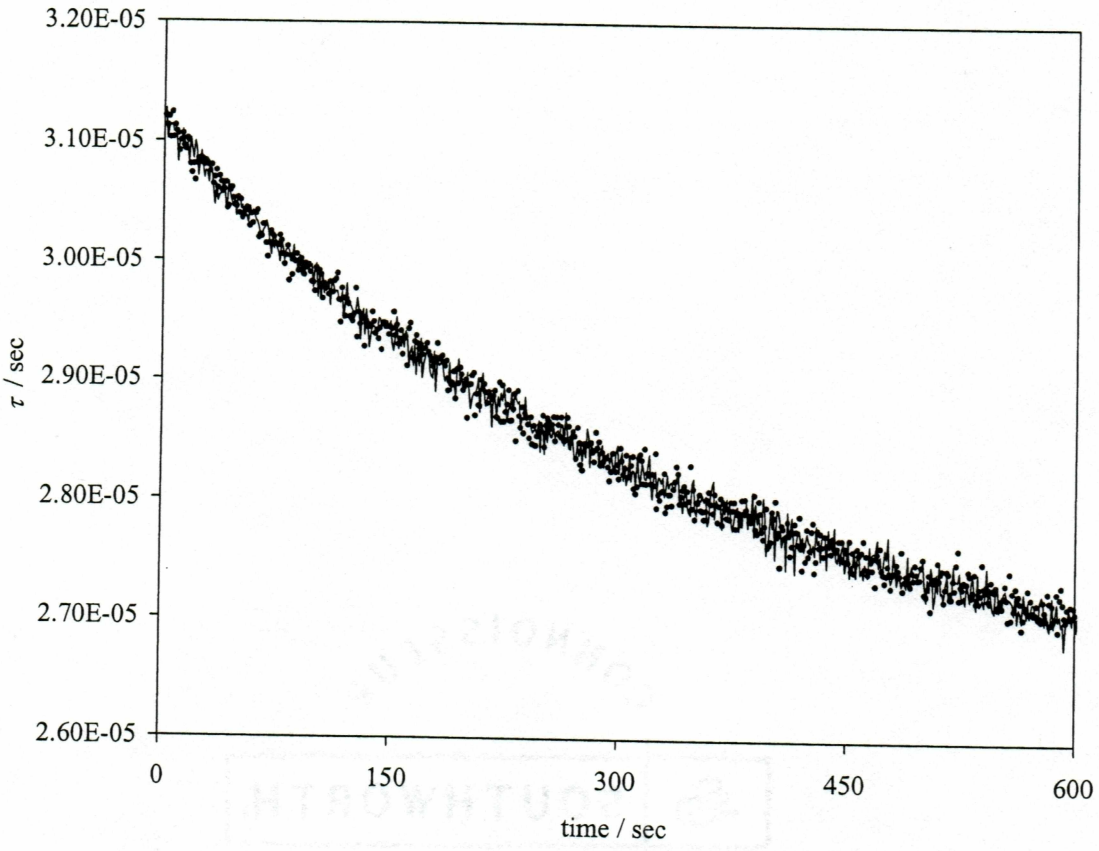

Figure 3.7 A ring-down time comparison between the UV light on and off states. The on states are represented by the line and the off states are represented by the black circles. The photolysis beam affects mirror reflectivity as shown by the decrease in τ.

UV light on and off bins is shown in figure 3.8. The noise for figure 3.8 is 5.7×10^{-9} cm^{-1} (1σ). From figure 3.8, it can be determined that Δr is inaffected by mirror reflectivity changes from the UV effect. In the program for data analysis, the averaging was manipulated to record more shots per data point while still maintaining 5 shots on and 5 shots off differencing to reduce the amount of noise. Using this data averaging allowed many points to be recorded and a lower detection limit to be achieved for the photolysis experiments.

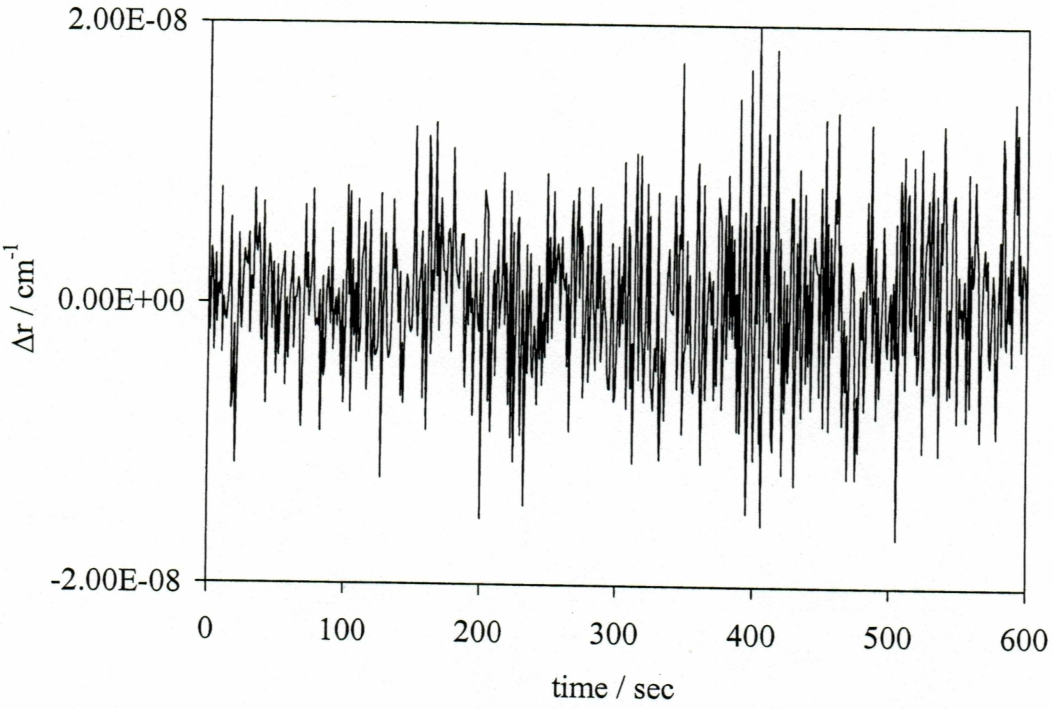

Figure 3.8 The change in loss rate, Δr, as a function of time. This figure represents the same data as figures 3.4 and 3.5. The effective noise for 5 shots on minus 5 shots off is 6×10^{-9} cm^{-1} (1σ).

Chapter 4
Calculations

4.1 Introduction

This chapter focuses on the calculations used for the determination of $\cdot NO_3$ quantum yield from PAN photolysis. The calculations used to determine the precursor number density and the $\cdot NO_3$ photoproduct number density using CRDS are discussed. Also, the calculations for the relative $\cdot NO_3$ quantum yield from PAN photolysis with corrections for the system design are described in this chapter.

4.2 Precursor number density calculation

The number densities for N_2O_5 and PAN delivered into the photolysis chamber were calculated from IR spectra. The known IR integrated band strengths, S', were presented in table 2.1 for PAN [*Gaffney et al.*, 1984] and the known IR cross section, ε, from *Wangberg et al.* [1997] for N_2O_5 at 1246 cm^{-1} is 8.56 x 10^{-19} cm^2 $molecule^{-1}$. The number density delivered to the chamber can be determined using two separate methods: the peak integration method and the peak height method.

In the peak height method, the absorbance at a peak maximum is used to determine the absolute concentration through Beer's Law. For N_2O_5, the height of the absorbance peak A at 1246 cm^{-1} was measured and with the known cross section, ε, a number density, N^{FTIR}, was determined,

$$A = -log\left(\frac{I}{I_o}\right) = \varepsilon N^{FTIR} l \,. \tag{4.1}$$

The path-length, l, is 17 cm for the IR cell.

The peak integration method was used to determine PAN's number density. The number density for PAN delivered to the photolysis chamber was determined by integrating the PAN absorption peaks at 1841, 1741, 1302, and 1163 cm^{-1}. The

calculated number density for the 1302 cm^{-1} peak was higher than the number density derived from the other PAN absorption peak integrations. A possible reason for the 1302 cm^{-1} peak not being quantitative was asymmetry in its peak shape, possibly caused by irregular baseline structure or another absorber. Therefore, the peak at 1302 cm^{-1} was not used in the number density calculation for PAN. In the peak integration method, the integral under an absorption feature was converted to a number density using an integrated form of Beer's law,

$$A_{peak} = \int A d\nu = S' N^{FTIR} l . \tag{4.2}$$

The A_{peak} is the absorption peak integration, S' is the integrated band strength and N^{FTIR} is the number density. The number density of PAN was averaged for the three separate absorption peaks to obtain more accurate values. The relative standard deviation between the PAN absorption peak integrations is 4%.

4.3 Nitrate radical ($\cdot NO_3$) number density calculation

The number density of $\cdot NO_3$ formed photolytically is determined using the peak absorption for $\cdot NO_3$ at 662 nm. For CRDS, the absorption of the molecule is calculated by the multiplying the ring-down time, τ, by the speed of light, and inverting it to give a loss rate, r. The change in loss rate due to photolysis, Δr, is determined by modulating the UV beam on and off and sorting the resulting ring-down times into on and off bins. The off bin, τ_{off}, represents a baseline from which the on bin, τ_{on}, can be subtracted,

$$\Delta r = \frac{1}{c\tau_{on}} - \frac{1}{c\tau_{off}} . \tag{4.4}$$

Sorting the ring-down loss rates into the on and off bins eliminates the problems of thermal decomposition of N_2O_5 forming $\cdot NO_3$ and mirror reflectivity variation with wavelength. Beer's law relates the change in loss rate, Δr, to the absorbance to determine the average number density of $\cdot NO_3$, $\overline{N}_{NO_3}$,

$$\Delta r = \sigma \overline{N}_{NO_3} . \tag{4.5}$$

The absorption cross section of $\cdot NO_3$, σ, is 2.1 x 10^{-17} cm^2 $molecule^{-1}$ at 662 nm [*Wayne et. al* 1991]. This σ is used to determine the number density of $\cdot NO_3$ formed from photolysis.

Cavity ring-down spectroscopy measures average concentrations within the cavity, but the photoproduct is only in a fraction of the cavity's volume. The actual number density in the photolytic volume is larger than the average number density by the ratio l/l_x where l is the mirror to mirror path-length and l_x is the crossing length of the CRDS beam and the photolysis beam,

$$N_{NO_3} = \overline{N}_{NO_3} \frac{l}{l_x}. \tag{4.6}$$

For the calculation of absolute $\cdot NO_3$ quantum yield from the photolysis of its precursors discussed in the next section, this correction factor applies.

4.4 Absolute $\cdot NO_3$ quantum yield calculation

The absolute method of determining the $\cdot NO_3$ quantum yield measures the concentration of $\cdot NO_3$ in reference to the concentration of excited precursors in the photolytic volume. The total number of photons absorbed in the photolytic volume is quantified from the photolysis pulse energy E. The total number of photons, n_T, is calculated using Plank's relationship,

$$n_T = \frac{\lambda E}{hc} \tag{4.7}$$

where h is Plank's constant, c is the speed of light, and λ is wavelength of the photolysis beam. The number of photons absorbed, n_A, is calculated in a series of steps beginning with Beer's law,

$$ln\left(\frac{I_o}{I}\right) = \sigma_{pre} N_{pre} l_x. \tag{4.8}$$

In equation 4.8, I_o/I is the ratio between the initial and transmitted light intensities, σ_{pre} is absorption cross section of the precursor at the photolytic wavelength, N_{pre} is the number

density of the precursor, and l_x is the crossing path-length. The number density of the precursor, N_{pre}, in the photolytic volume is corrected for the diluting sidearm flow as discussed in chapter 3 and also a pressure change between the IR cell, p_{cell}, and chamber p_{cham},

$$N_{pre} = N_{pre}^{FTIR} \frac{F_{main} p_{cham}}{(0.5F_{purge} + F_{main}) p_{cell}}. \tag{4.9}$$

The F_{purge} is the purge flow, F_{main} is the main flow, and N_{pre}^{FTIR} is the number density determined from IR spectroscopy. The differential with respect to l_x of equation 4.8 is calculated to determine the photons absorbed in the crossing path-length l_x,

$$\frac{dI}{dl_x} = -I_o N_{pre} \sigma_{pre} e^{-N_{pre}\sigma_{pre} l_x}. \tag{4.10}$$

With weak absorbance of the photons per unit length, the e term is approximately 1, therefore,

$$\frac{n_a}{l_x} = -\frac{dI}{dl_x} = I_o N_{pre} \sigma_{pre}. \tag{4.11}$$

The molecular absorption of these photons takes place within a volume in the cavity that is determined by the photolysis beam area, A_{beam}, multiplied by l_x. The beam area, A_{beam}, is determined by measuring the height and width of the photolysis beam. Assuming the fluence (density of photons) is even across the laser beam, the photons absorbed per length, n_a, divided by A_{beam} determines the average number of photons absorbed in the crossing volume, N_a,

$$\frac{n_a}{l_x A_{beam}} = N_a \approx \left(\frac{n_T}{A_{beam}} \right) N_{pre} \sigma_{pre}. \tag{4.12}$$

The absorbed photon number density equals the excited precursor number density, thus the $\cdot NO_3$ quantum yield from the photolysis of the precursor is defined by,

$$\phi_{NO_3} = \frac{N_{NO_3}}{N_a}. \tag{4.13}$$

Equation 4.13 can be solved by substituting in F_{main} and F_{purge} from equation 4.9, A_{beam}, σ_{pre}, N_{pre}, and Plank's relationship (equation 4.7). The average $\cdot NO_3$ number density, $\overline{N}_{NO_3}$, determined by CRDS with the cavity path-length correction (equation 4.6) substituted for N_{NO_3} in equation 4.13 determines an absolute $\cdot NO_3$ quantum yield,

$$\phi_{NO_3} = \frac{\overline{N}_{NO_3}\left(0.5F_{purge} + F_{main}\right)p_{cell}hclA_{beam}}{F_{main}p_{cham}\sigma_{pre}N_{pre}\lambda El_x}. \tag{4.14}$$

The next section discusses the relative method used to determine the $\cdot NO_3$ quantum yield from PAN photolysis. Using the relative method relaxes assumptions such as equal laser fluence and equal flows into the side-arms.

4.5 Relative $\cdot NO_3$ quantum yield calculation

The relative $\cdot NO_3$ quantum yield from PAN photolysis calculation involves dividing the absolute PAN quantum yield equation, $\phi_{NO_3}(PAN)$, by the absolute N_2O_5 quantum yield equation, $\phi_{NO_3}(N_2O_5)$, when performing the same analysis for both precursors,

$$\frac{\phi_{NO_3}(PAN)}{\phi_{NO_3}(N_2O_5)} = \frac{\dfrac{\overline{N}_{NO_3}(PAN)\left(0.5F_{purge} + F_{main}\right)p_{cell}hclA_{beam}}{F_{main}p_{cham}\sigma_{PAN}N_{pre}^{FTIR}(PAN)\lambda El_x}}{\dfrac{\overline{N}_{NO_3}(N_2O_5)\left(0.5F_{purge} + F_{main}\right)p_{cell}hclA_{beam}}{F_{main}p_{cham}\sigma_{N_2O_5}N_{pre}^{FTIR}(N_2O_5)\lambda l_x}}. \tag{4.15}$$

Equation 4.15 can be reduced and solved for $\phi_{NO_3}(PAN)$,

$$\varphi_{NO_3}(PAN) = \phi_{NO_3}(N_2O_5)\frac{\overline{N}_{NO_3}(PAN)\sigma_{N_2O_5}N_{pre}^{FTIR}(N_2O_5)}{\overline{N}_{NO_3}(N_2O_5)\sigma_{PAN}N_{pre}^{FTIR}(PAN)}. \tag{4.16}$$

Using this relative method eliminates l_x, l, F_{tot}, F_{main}, h, c, λ, E, and A_{beam} from the quantum yield equation. With $\phi_{NO_3}(N_2O_5)$ at 289 nm equal to 1 [*DeMore et al.*, 1997], the relative quantum yield of PAN can be determined without having to use many variables that can lead to inaccurate quantum yield results. This relative method was used to determine the $\cdot NO_3$ quantum yield from PAN photolysis. The next chapter discusses these results.

Chapter 5
Results

5.1 Introduction

This chapter discusses the observed $\cdot NO_3$ quantum yield from N_2O_5 photolysis using the experimental system. The results from N_2O_5 photolysis are compared to the recommended $\cdot NO_3$ quantum yield literature value of 1 near 289 nm. This chapter also reports the $\cdot NO_3$ quantum yield from PAN photolysis at a wavelength of 289 nm.

5.2 Absolute quantum yield determination of $\cdot NO_3$ from N_2O_5 photolysis

The absolute $\cdot NO_3$ quantum yield method described in section 4.4 was used to check the experimental system's operation. The system was not designed to measure absolute quantum yields because large uncertainties exist in experimental parameters. Therefore the absolute method was only used to check that the results are within the same order of magnitude as the literature recommended value. Dependence on the unknown experimental parameters that limit the utility of the absolute method cancels in the relative method, which is why we only use the relative method to measure PAN quantum yields.

The absolute $\cdot NO_3$ quantum yield from N_2O_5 photolysis was determined using equation 4.1 and the experimental parameters listed in table 5.1 including the N_2O_5 number density for the first N_2O_5 experiment, N_2O_5_1. All errors listed in table 5.1 are 1σ. One IR absorption spectrum (1A) was recorded during the middle of the experiment for N_2O_5_1. The fractional uncertainty (6.6%) used in the N_2O_5_1 number density determination obtained from the third N_2O_5 experiment (N_2O_5_3) that had three N_2O_5 number density values as shown in table 5.2. The errors listed in table 5.2 are also 1σ. The number densities listed in table 5.2 are also used to calculate the relative $\cdot NO_3$ quantum yield from PAN photolysis as discussed later.

Table 5.1 Experimental parameters used to determine the absolute $\cdot NO_3$ quantum yield from N_2O_5 photolysis.

experimental parameter	unit	Value
F_{purge}	sccm	100
F_{main}	sccm	100
p_{cham}	Torr	10.4
p_{cell}	Torr	26.3
l	cm	50
l_x	cm	8.1 †
l_{beam}	cm	0.30 ± 0.10
w_{beam}	cm	0.15 ± 0.05
A_{beam} *	cm^2	0.045 ± 0.010
λ	nm	289
$\sigma_{N_2O_5}$ ‡	cm^2 $molec^{-1}$	7.4×10^{-20}
$N_{N_2O_5}^{FTIR}$	molec cm^{-3}	$[6.04 \pm 0.27] \times 10^{14}$
$\overline{N}_{NO_3}$ (N_2O_5_1)	molec cm^{-3}	$[2.08 \pm 0.04] \times 10^{10}$
E	J	$[1.0 \pm 0.5] \times 10^{-3}$

* The A_{beam} was calculated by multiplying the width of the beam, w_{beam}, by the length of the beam, l_{beam}.

† Although this number is likely to have a large error, we are unable to estimate its magnitude.

‡ Value from *DeMore et al.* [1997].

Table 5.2 Calculated number densities of N_2O_5. The N_2O_5 was delivered into the vacuum chamber for determining the absolute $\cdot NO_3$ quantum yield from N_2O_5 photolysis and the relative $\cdot NO_3$ quantum yield from PAN photolysis. See text for discussion on the N_2O_5 selected number density determination.

IR spectrum	N_2O_5 number density molec cm^{-3}	N_2O_5 selected density molec cm^{-3}
1A	6.04×10^{14}	$[6.04 \pm 0.40] \times 10^{14}$
2A	7.06×10^{14}	$[4.82 \pm 0.32] \times 10^{14}$
2B	4.82×10^{14}	
3A	4.21×10^{14}	$[4.05 \pm 0.27] \times 10^{14}$
3B	4.21×10^{14}	
3C	3.74×10^{14}	

Figure 5.1 shows a raw data plot for $\cdot NO_3$ formed *via* N_2O_5 photolysis. In figure 5.1, the solid line represents the UV light on state and the dashed line represents the UV light off state. The general increase in the loss rate, r, at longer wavelengths is due to a decrease in mirror reflectivity. The absorption peak centered at 662 nm for $\cdot NO_3$ was used for determining the $\cdot NO_3$ number density formed *via* photolysis. The absorbance of $\cdot NO_3$ centered at 662 nm for the UV off loss rate is $\cdot NO_3$ produced by N_2O_5 thermal decomposition. The UV off loss rate was subtracted from the UV on loss rate to determine Δr. Figure 5.2 shows the difference in loss rate between the UV on and off states, Δr, represented by the circles. The solid line in figure 5.2 represents a $\cdot NO_3$ reference absorption cross section spectrum [*Wayne et al.*, 1991] that is proportional to Δr as given by equation 4.5. The difference in loss rate is the photolytic $\cdot NO_3$ absorption that was used to calculate the $\cdot NO_3$ number density in the quantum yield determination (equation 4.14). The number density of $\cdot NO_3$ formed *via* N_2O_5 photolysis for N_2O_5_1, $\overline{N}_{NO_3}$, is [2.08 ± 0.04] x 10^{10} molec cm^{-3}. The error estimate was calculated by fitting the observed Δr spectrum to the reference spectrum with a non-linear least squares fitting routine that reported the standard deviation of the fit parameters (Igor Pro, Wavemetrics Inc.).

The $\cdot NO_3$ quantum yield from N_2O_5 photolysis was experimentally determined to be 0.34 ± 0.26 for N_2O_5_1. This quantum yield value provided a estimate for the efficiency of the photolysis system. However, the experimentally derived value is low compared to the recommended quantum yield value at 289 nm of 1 for N_2O_5 [*DeMore et al.*, 1997]. This difference is due to several factors that are difficult to quantify in the absolute quantum yield method. Photolysis beam and probe beam misalignment can lead to misestimation of the photolytic crossing region, l_x. We feel that this misalignment caused

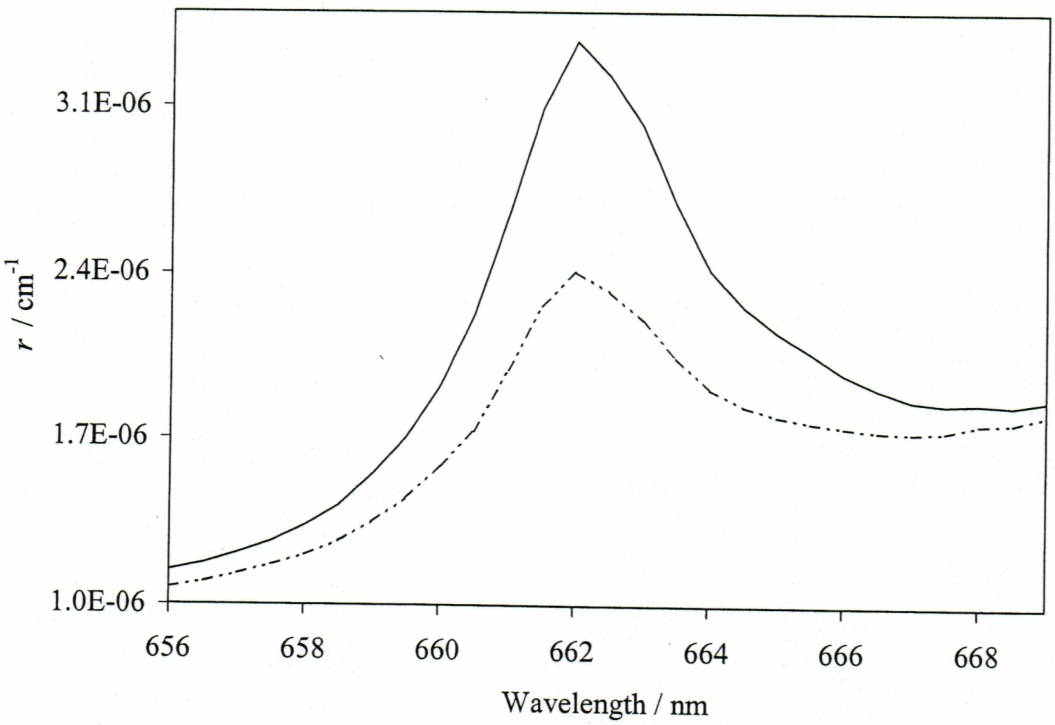

Figure 5.1 Raw data plot showing $\cdot NO_3$ formed from N_2O_5 photolysis. The maximum absorbance of $\cdot NO_3$ is centered at 662 nm. The solid line represents the photolysis beam on state and the dashed line represents the photolysis beam off state. Thermal decomposition of N_2O_5 into $\cdot NO_3$ accounts for the absorption seen in the UV off state.

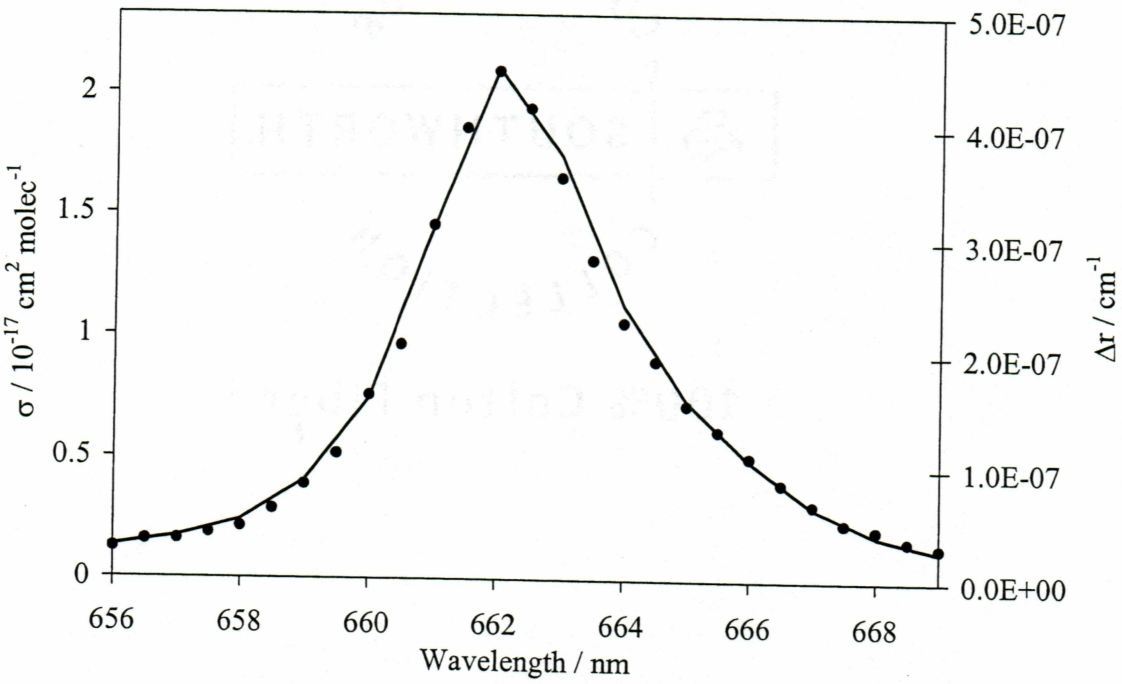

Figure 5.2 Spectrum of $\cdot NO_3$ formed from N_2O_5 photolysis. The change in loss rate, Δr, is represented by the circles and the $\cdot NO_3$ experimental absorption cross section spectrum from *Wayne et al.* [1991] is represented by the line.

the largest amount of error in the absolute quantum yield quantification. Other errors that can lead to underestimation of ϕ_{NO_3} (N_2O_5) include an underestimated purge flow dilution and photolysis beam area, A_{beam}. A combination of these factors is most likely responsible for the low observed quantum yield value. However, as discussed in chapter 4, using a relative method for $\cdot NO_3$ quantum yield from PAN photolysis determination eliminates these estimation errors.

5.3 Relative quantum yield determination of $\cdot NO_3$ from PAN photolysis

The $\cdot NO_3$ quantum yield from PAN photolysis was determined using equation 4.16, the calculated N_2O_5 number densities in table 5.2, and the PAN number densities in table 5.3. All errors in table 5.3 are 1σ. In table 5.2, experiment N_2O_5_1 had one absorption spectrum. In the second experiment, liquid N_2 was added to the chloroform slush bath between first IR spectrum (2A) and and the second IR spectrum (2B) to keep the slush bath cool. This cooling decreased the vapor pressure of N_2O_5 leading to a decrease N_2O_5 number density. Spectrum 2B better represents the N_2O_5 number density because spectrum 2B was recorded at the $\cdot NO_3$ absorption peak near 662 nm. Spectrum 2A was not figured into the N_2O_5 number density because it was recorded before the liquid N_2 was added. The third experiment, N_2O_5_3, contained a set of IR spectra taken at the beginning (3A; about 655 nm - 660 nm), middle (3B; about 660 nm - 665 nm) and end (3C; about 665 nm -669 nm) of the photolysis experiment when scanning over wavelength for $\cdot NO_3$ determination. From these spectra, the average number density calculated from the three IR spectra was chosen as the representative number density. During the photolysis experiments for PAN, the first IR absorption spectrum was recorded at the beginning of the experiment (1A; 2A), the second spectrum was recorded during the middle (1B; 2B), and the third spectrum was taken at the end of the experiment (1C; 2C). Using this method determined if any fluctuations occurred in PAN

Table 5.3 Calculated number densities of PAN. The PAN was delivered into the chamber for the relative $\cdot NO_3$ quantum yield determination from PAN photolysis. See text for discussion.

IR spectrum	PAN number density molec cm^{-3}	PAN selected density molec cm^{-3}
1A	7.17×10^{14}	$[5.81 \pm 1.25] \times 10^{14}$
1B	5.53×10^{14}	
1C	4.71×10^{14}	
2A	4.77×10^{14}	$[4.28 \pm 0.47] \times 10^{14}$
2B	4.27×10^{14}	
2C	3.82×10^{14}	

concentration. The three number densities recorded were then averaged to determine the number density of PAN used in equation 4.16 for calculating the quantum yield result.

For the relative quantum yield determinations, the carrier gas switched between N_2O_5 and PAN samples. The N_2O_5 flowed into the chamber before and after PAN. Using this method allowed photolysis data for N_2O_5 to be averaged and compared with PAN data. The data was interpolated allowing for experimental variations (*i.e.* laser power, temperature, etc.) to be compensated for between N_2O_5 and PAN experiments leading to less error. Scans across wavelengths from 655 nm to 669 nm were taken for the respective precursor flows. A $\cdot NO_3$ absorption spectrum formed from PAN photolysis is shown in figure 5.3 with a $\cdot NO_3$ reference spectrum [*Wayne et al.*, 1991] of the absorption cross section shown for comparison. The precursor number density ratios, loss ratios, and quantum yield values are listed in table 5.4. All errors in table 5.4 are 1σ. At 289 nm, σ_{PAN} is 5.95 x 10^{-21} cm^2 $molec^{-1}$ [*Talukdar et al.*, 1995]. The $\cdot NO_3$ quantum yield from PAN photolysis was determined to be 0.30 ± 0.08 at a photolysis wavelength of 289 nm. The 289 nm photolysis of PAN quantum yield result is at, effectively, the highest energy and lowest wavelength available for atmospheric photolysis.

In summary, the absolute $\cdot NO_3$ quantum yield determination from N_2O_5 photolysis is measured to be 0.34 ± 0.26 which is low compared to the literature value of 1 [*DeMore et al.*, 1997]. Inaccurate measurements of the photolytic crossing region, l_x, or dilution flows are the most likely causes of this discrepancy. However, it should be noted that the system was not designed for absolute quantum yield measurements. Thus, a relative method is better suited for PAN quantum yield measurements using this system. This thesis also reports for the first time that the $\cdot NO_3$ quantum yield from PAN photolysis at 289 nm is 0.30 ± 0.08. The next chapter discusses this work in the context of previous work on PAN photolysis.

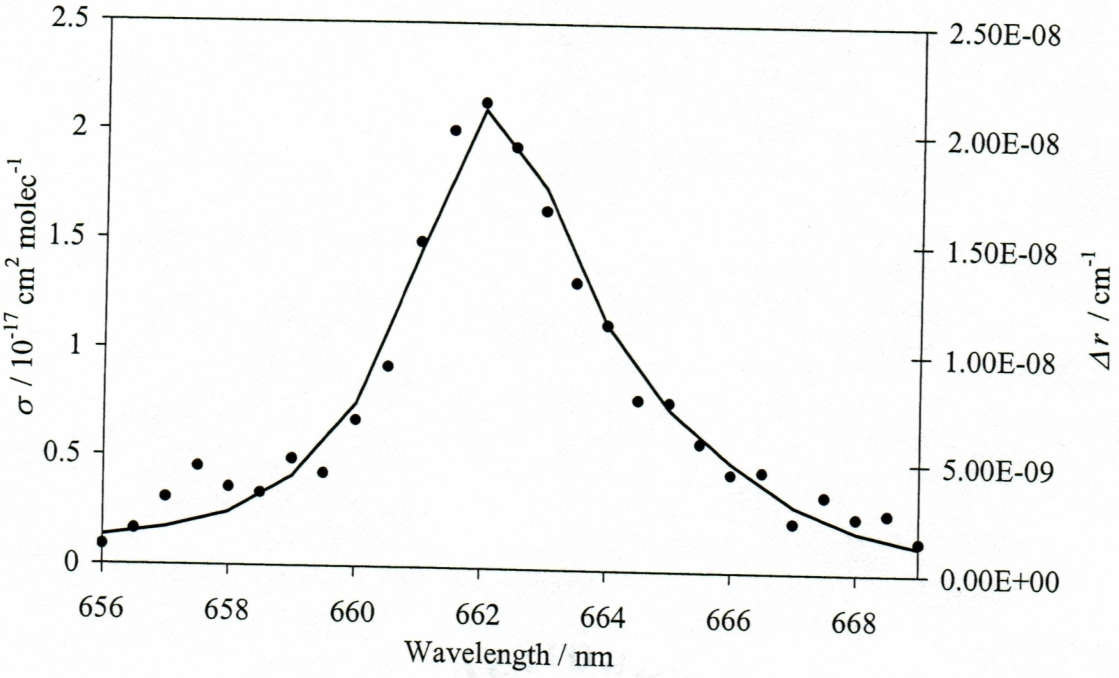

Figure 5.3 Spectrum of $\cdot NO_3$ from PAN photolysis. The change in loss rate, Δr, is represented by the circles and the reference $\cdot NO_3$ spectrum from *Wayne et al.* [1991] is represented by the line.

Table 5.4 Relative $\cdot NO_3$ quantum yield determination from PAN photolysis data. The $\cdot NO_3$ number density from N_2O_5 photolysis was interpolated by averaging the amount of $\cdot NO_3$ formed for the two N_2O_5 experiments relative to the PAN experiments. The number density ratio was calculated by averaging the N_2O_5 number densities relative to the PAN experiments

Experiment	$\overline{N}_{NO_3}$ molec cm^{-3}	$\overline{N}_{NO_3}$ (N_2O_5) interp molec cm^{-3}	Number density ratio N_2O_5/PAN	$\cdot NO_3$ quantum yield from PAN
N_2O_5_1	$[2.08 \pm 0.04] \times 10^{10}$			
PAN_1	$[6.67 \pm 0.30] \times 10^{8}$	$[2.75 \pm 0.08] \times 10^{10}$	0.93 ± 0.22	0.28 ± 0.07
N_2O_5_2	$[3.42 \pm 0.08] \times 10^{10}$			
PAN_2	$[9.55 \pm 0.36] \times 10^{8}$	$[3.96 \pm 0.10] \times 10^{10}$	1.04 ± 0.15	0.31 ± 0.05
N_2O_5_3	$[4.49 \pm 0.05] \times 10^{10}$			

Chapter 6
Discussion and Conclusion

6.1 Introduction

This chapter discusses the $\cdot NO_3$ quantum yield from PAN photolysis results. We consider two limiting mechanisms for PAN photodissociation. Results from this work and previous work are discussed in the context of these mechanisms. This chapter also describes future studies on the $\cdot NO_3$ quantum yield from PAN.

6.2 Discussion

In general, we can consider two limiting mechanisms for a photodissociation process, a direct mechanism and an indirect mechanism. In the mechanism of direct photodissociation, the excited state dissociates into products due to the repulsive nature of the excited electronic state. If a single excitation promotes an electron from a bonding to an anti-bonding orbital the excited state is then repulsive along the coordinate affected by the excited molecular orbital. If multiple excited states exist and if more than one state absorbs at a certain wavelength, then each of these excited states can lead to different photoproducts. Therefore, a non-unity quantum yield for a specific product would be indicative of multiple direct dissociation pathways occurring at the same wavelength. Because each excited state will have a different absorption maximum, tuning the photolysis wavelength will tune the fraction of absorption from each directly dissociating state. Thus, in the case of direct photodissociation, the quantum yield for a specific product is typically a function of wavelength.

In the other mechanism, indirect photodissociation, the excited state lives long enough to distribute the photoexcitation energy into all vibrational modes of the molecule. Typically, the weakest bond in the molecule is broken. In the case of a molecule that has two equally weak bonds, the quantum yield indicates that the weak

bonds break with nearly equal ratios. In this mechanism, the quantum yield typically does not depend on wavelength unless the photon's energy is low enough to make one pathway energetically inaccessible. The bond strengths between O-O and N-O in PAN are nearly equal [*Miller et al.*, 1999]. This mechanism therefore predicts nearly equal quantum yields between $\cdot NO_2$ and $\cdot NO_3$. The energy of light corresponding to the light's photolysis wavelength in this study is higher than both bond energies so the $\cdot NO_2$ and $\cdot NO_3$ quantum yields would remain the same until the molecule does not absorb light.

An example that illustrates atmospheric photochemistry relating to PAN and the two mechanisms well is ozone photodissociation,

$$O_3 + h\nu \rightarrow O_2 + O\,. \tag{6.1}$$

In this case, two possible spin-orbit states of the oxygen atom are formed, $O(^3P)$ and $O(^1D)$. It had been assumed that O_3 photolysis forms all products with singlet electronic states because O_3 exists as a singlet; therefore $O(^1D)$ must be formed with $O_2(^1\Delta)$ and $O(^3P)$ with $O_2(^3\Sigma)$. We later question this simplifying assumption. The energy required to break the $O\text{-}O_2$ bond plus produce excited oxygen molecule, $O_2(^1\Delta)$, and a singlet oxygen atom, $O(^1D)$, requires a threshold energy of light approximately equivalent to 310 nm [*Finlayson-Pitts and Pitts*, 2000]. Therefore we expect repulsive electronic states leading to $O(^1D)$ and $O_2(^1\Delta)$ absorb light at wavelengths less than 310 nm while lower electronic states leading to $O(^3P)$ and $O_2(^3\Sigma)$ absorb at wavelengths greater than 310 nm. Two bands are observed in the absorption spectrum: the Hartley band (< 300 nm) and the Huggins band (> 300 nm). Absorption of light in the Hartley band typically corresponds to $O(^1D)$ formation and absorption in the Huggins band typically corresponds to $O(^3P)$ formation. At first glance, the observations agree with this simple model; $O(^1D)$ forms with high quantum yield at wavelengths less than 310 nm, and low quantum yields at longer wavelengths.

Subtle effects are also seen in O_3 photodissociation leading to differences in the $O(^1D)$ quantum yield model. The production of $O(^1D)$ from O_3 photolysis has been considered by *Michelsen et al.* [1994] who theorized that $O(^1D)$ can be produced at wavelengths longer than the energetic cutoff corresponding to 310 nm. The observed quantum yield of $O(^1D)$ is about 0.2 at 315 nm. This $O(^1D)$ production observed in the Huggins band is partially due to a "hot-band" absorption of O_3 where the O_3 molecule contains additional rovibrational energy that helps overcome the wavelength threshold. *Takahashi et al.* [1996] also observed a spin-forbidden pathway for the formation of $O(^1D)$ in the 317 - 327 nm wavelength region. In the spin forbidden process, O_3 photolysis yields $O(^1D)$ and $O_2(^3\Sigma)$ photoproducts. Also, at shorter wavelengths (< 280 nm) the $O(^1D)$ quantum yield decreases slightly. This decrease is not fully understood. *Wayne* [1987] theorizes that the upper electronic states initially populated on light absorption contain a curve crossing with a repulsive state that corresponds to $O(^3P)$ production. Population of these repulsive states need higher energies that correspond to shorter wavelengths. From the example of O_3 photodissociation, it is important to understand that multiple electronic photodissociative pathways can exist for molecules such as PAN leading to non-unity quantum yield values.

The quantum yield result from this work, $\phi_{NO_3}(PAN)$ is 0.30 ± 0.08 at 289 nm, is in good agreement with the previous result from *Mazely et al.* [1997] of 0.3 ± 0.1 at 248 nm. Recently *Harwood et al.* [2003] reported the $\cdot NO_3$ quantum yields from PAN photolysis at 248 and 308 nm to be 0.19 ± 0.04 and 0.41 ± 0.10, respectively. Our work provides an intermediate value between the wavelengths measured by *Harwood et al.* [2003]. The quantum yield changes from 0.19 ± 0.04 at 248 nm to 0.41 ± 0.10 at 308 nm. From the comparison to *Harwood et al.* [2003], PAN can possibly contain multiple excited states leading to a wavelength dependent direct photodissociation. However, the

bond energy difference between the O-O and the N-O bond is small leading to either bond breaking, consistent with an indirect mechanism. Therefore the photodissociation of PAN contains properties indicative of both limiting mechanisms.

6.3 Future studies

The wavelength dependence of the $\cdot NO_3$ quantum yield can be further studied by photolyzing PAN at wavelengths longer than 289 nm. The absorption cross section of PAN decreases with wavelength possibly leading to less $\cdot NO_3$ production. However, stronger light intensities exist at longer wavelengths in the atmosphere possibly leading to higher photolysis rates. Other excited states might exist that are accessible at longer wavelengths leading to changes in the quantum yield.

Other members of the peroxy nitrate (PN) family can be photolyzed with the photolysis system. Peroxypropionyl nitrate (PPN) photolysis could be an interesting experiment because it is the second most abundant PN compound in the environment. *Harwood et al.* [2003] reports $\phi_{NO_3}(PPN)$ is 0.22 ± 0.04 and 0.39 ± 0.04 at 248 nm and 308 nm respectively. These results are indicative of a possible wavelength dependent mechanism for PPN photolysis. Peroxybenzoyl nitrate (PBzN) could also be studied because the C_6H_5 functional group is more electron withdrawing than the CH_3 functional group. This substitution could lead to different $\cdot NO_3$ quantum yield values for PBzN and PAN due to the different photodissociative mechanisms discussed.

Further analysis of $\cdot NO_3$ quantum yields from PAN should include determining pressure dependence. Molecular quenching could affect the $\cdot NO_3$ quantum yield results for PAN photolysis so the pressure dependence, if any, needs to be examined. Using the photolysis chamber, the pressure can be adjusted to copy atmospheric pressures to determine the altitude dependence of the $\cdot NO_3$ quantum yield value of PAN.

We look forward to using the photolysis system to gain a better mechanistic understanding of peroxy nitrate family photochemistry and its importance in the atmosphere.

References

AMAP Working Group, *Arctic Pollution 2002: Persistent Organic Pollutants, Heavy Metals, Radioactivity, Human Health, Changing Pathways*, Arctic Monitoring and Assessment Programme, Oslo, Norway, 2002.

Beine, H.J., D.A. Jaffe, D.R. Blake, E. Atlas, and J. Harris, Measurements of PAN, alkyl nitrates,ozone, and hydrocarbons during spring in interior Alaska, *J. Geophys. Res.*, **101** (D7), 12613-12619, 1996.

Beine, H.J., and T. Kroges, The seasonal cycle of peroxyacetyl nitrate (PAN) in the European Arctic, *Atmos. Environ.*, **34**, 933-940, 2000.

Bottenheim, J.W., L.A. Barrie, and E. Atlas, The paritioning of nitrogen oxides in the lower arctic troposphere during spring 1988, *J. Atmos. Chem.*, **17**, 15-27, 1993.

Bridier, I., F. Caralp, H. Loirat, R. Lesciaux, B. Veyret, K.H. Becker, A. Reamer, and F. Zabel, Kinetic and theoretical studies of the reactions $CH_3C(O)O_2 + NO_2 + M \equiv CH_3C(O)O_2NO_2 + M$ between 248 and 393 K and between 30 and 760 torr, *J. Phys Chem*, **95**, 3594-3600, 1991.

Busch, K.W., and M.A. Busch, *Cavity ring-down spectroscopy: an ultratrace-absorption measurement technique*, American Chemical Society, Washington, DC, 1999.

Dick, E., *The application of cavity ring-down spectroscopy to determine nitrate radical concentrations in the atmosphere*, M.S. thesis, University of Alaska Fairbanks, Fairbanks, 2002.

DeMore, W.B., S.P. Sander, D.M. Golden, R.F. Hampson, M.J. Kurylo, C.J. Howard, A.R. Ravishankara, C.E. Kolb, and M.J. Molina, *Chemical Kinetics and Photochemical Data for use in Stratospheric Modeling, Eval. No. 12*, J.P.L. Publications, Pasedena, CA, 1997.

Finlayson-Pitts, B.J., and J.N. Pitts, *Chemistry of the Upper and Lower Atmosphere*, Academic Press, San Diego, 2000.

Gaffney, J.S., R. Fajer, and G.I. Senum, An improved procedure for high purity gaseous peroxyacyl nitrate production: Use of heavy lipid solvents, *Atmos Environ.*, **18** (1), 215-218,1984.

Grosjean, D.E., E. Grosjean, and E.L. Williams, II, Thermal decomposition of PAN, PPN, and vinyl-PAN, *J. Air Waste Manage. Assoc.*, **44**, 391-396, 1994.

Harwood, M.H., J.M. Roberts, G.J. Frost, A.R. Ravishankara, and J.B. Burkholder, Photochemical studies of $CH_3C(O)OONO_2$ (PAN) and $CH_3CH_2C(O)OONO_2$ (PPN): NO_3 quantum yields, *J. Phys Chem. A*, **107**, 1148-1154, 2003.

Holmes, J.R., Peroxyacetyl nitrate (PAN) measurements in the south coast air basin of California, Research Note No. 89-4, California Environmental Protection Agency, May 1989.

Jacob, D.J., B.G. Heikes, S.M. Fan, J.A. Logan, D.L. Mauzerall, J.D. Bradshaw, H.B. Singh, G.L. Gregory, R.W. Talbot, D.R. Blake, and G.W. Sachse, Origin of ozone and NO_x in the tropical troposphere: A photochemical analysis of aircraft observations over the South Atlantic basin, *J. Geophys. Res.*, **101** (D19), 24235-24250, 1996.

King, M.D., Dick, E.M., and W.R. Simpson, A new method for the atmospheric detection of the nitrate radical (NO_3), *Atmos. Environ.*, **34**, 685-688, 2000.

Libuda, H.G. and F. Zabel, UV absorption cross sections of acetyl peroxynitrate and trifluoroacetyl peroxynitrate at 298 K, *Ber. Bunsenges. Phys. Chem.*, **99** (10), 1205-1213, 1995.

Mazely, T.L., R.R. Friedl, and S.P. Sander, Quantum yield of NO_3 from peroxyacetyl nitrate photolysis, *J. Phys. Chem. A*, **101**, 7090-7097, 1997.

Miller, C.E., J.L. Lyton, D.M. Keevil, and J.S. Francisco, Dissociation pathways of peroxyacetyl nitrate, *J. Phys. Chem. A*, **103**, 11451-11459, 1999.

Moxim, W.J., H. Levy II, and P.S. Kasibhatla, Simulated global tropospheric PAN: Its transport and impact on NO_x, *J. Geophys. Res.*, **101** (D7), 12621-12638, 1996.

Orlando, J.J., G.S. Tyndall, and J.G. Calvert, Thermal decomposition pathways for peroxyacetyl nitrate (PAN): Implifications for atmospheric methyl nitrate levels, *Atmos. Environ.*, **26A** (17) 3111-3118, 1992.

Prinn, R.G., J. Huang, R.F. Weiss, D.M. Cunnold, P.J. Fraser, P.G. Simmonds, A. McCulloch, C. Harth, P. Salameh, S. O'Doherty, R.H.J. Wang, L. Porter, B.R. Miller, Evidence for substantial variations of atmospheric hydroxyl radicals in the past two decades, *Science*, **292**, 1882-1888.

Ravishankara, A.R., P.H. Wine, C.A. Smith, P.E. Barbone, and A. Torabi, N_2O_5 photolysis: Quantum yields for NO_3 and $O(^3P)$, *J. Geophys. Res.*, **91** (D5), 5355-5360, 1986.

Roberts, J.M., S.B. Bertman, D.D. Parrish, F.C. Fehsenfeld, B.T. Jobson, and H. Niki, Measurement of alkyl nitrates at Chebogue Point, Nova Scotia during the 1993 North Atlantic Regional Experiment (NARE) intensive, *J. Geophys. Res.*, **103** (D11), 13569-13580, 1998.

Swanson, D., B. Kan, and H.S. Johnston, NO_3 quantum yields from N_2O_5 photolysis, *J. Phys. Chem.*, **88**, 3115-3118,1984.

Singh, H.B., Reactive nitrogen in the troposphere, *Environ. Sci. Technol.*, **21** (4), 320-327, 1987.

Simpson, W.R., Continous wave cavity ring-down spectroscopy applied to *in situ* detection of dinitrogen pentoxide (N_2O_5), *Rev. Sci. Instrum.*, **74** (7), 2003 in press.

Stephens, E.R., Smog studies of the 1950s, *EOS*, **68** (7), 89, 91-93, 1987.

Takahashi, K., Kishigami, M., Matsumi, Y., Kawasaki, M., and A. Orr-Ewing, Observation of the spin-forbidden $O(^1D) + O_2(^3\Sigma)$ channel in the 317-327 nm photolysis of ozone, *J. Chem. Phys.*, **105** (12), 5290-5293, 1996.

Talukdar, R.K., J.B. Burkholder, A.M. Schmoltner, J.M. Roberts, R.R. Wilson, and A.R. Ravishankara, Investigations of the loss process for peroxyacetyl nitrate in the atmosphere: UV photolysis and reaction with OH, *J. Geophys. Res.*, **100** (D7), 14163-14713, 1995.

Trost, B., *Nitrogen oxide photochemistry in marine air over the Eastern Pacific*, M.S. thesis, University of Alaska Fairbanks, Fairbanks, 2000.

Walega, J.G., B.A. Ridley, S. Madronich, F.E. Grahek, J.D. Shetter, T.D. Sauvain, C.J. Hahn, J.T. Merill, B.A. Bodhaine, and E. Robinson, Observations of peroxyacetyl nitrate, peroxypropionyl nitrate, methyl nitrate, and ozone during the Mauna Loa Observatory photochemistry experiment, *J. Geophys. Res.*, **97** (D10), 10311-10330, 1992.

Wangberg, I., T. Etzkorn, I. Barnes, U. Platt, and K.H. Becker, Absolute determination of the temperature behavior of the $NO_2 + NO_3 + (M) \equiv N_2O_5 + (M)$ equilibrium, J. *Phys. Chem A.*, **101**, 9694-9698, 1997.

Wayne, R.P., The photochemistry of ozone, *Atmos. Environ.*, **21** (8), 1683-1694, 1987.

Wayne, R.P., I. Barnes, P. Biggs, J.P. Burrows, C.E. Canosa-Mas, J. Hjorth, G. Le Bras, G.K. Moortgat, D. Perner, G. Poulet, G. Restelli, and H. Sidebottom, The nitrate radical: physics, chemistry, and the atmosphere, *Atmos. Environ.*, **25A** (1), 1991.